Propagation of intense short laser pulses in the atmosphere

P. Sprangle,[1] J. R. Peñano,[1] and B. Hafizi[2]
[1]*Plasma Physics Division, Naval Research Laboratory, Washington, DC 20375*
[2]*Icarus Research, Inc., P.O. Box 30780, Bethesda, Maryland 20824-0780*
(Received 26 February 2002; published 30 October 2002)

The propagation of short, intense laser pulses in the atmosphere is investigated theoretically and numerically. A set of three-dimensional (3D), nonlinear propagation equations is derived, which includes the effects of dispersion, nonlinear self-focusing, stimulated molecular Raman scattering, multiphoton and tunneling ionization, energy depletion due to ionization, relativistic focusing, and ponderomotively excited plasma wakefields. The instantaneous frequency spread along a laser pulse in air, which develops due to various nonlinear effects, is analyzed and discussed. Coupled equations for the power, spot size, and electron density are derived for an intense ionizing laser pulse. From these equations we obtain an equilibrium for a single optical-plasma filament, which involves a balancing between diffraction, nonlinear self-focusing, and plasma defocusing. The equilibrium is shown to require a specific distribution of power along the filament. It is found that in the presence of ionization a self-guided optical filament is not realizable. A method for generating a remote spark in the atmosphere is proposed, which utilizes the dispersive and nonlinear properties of air to cause a low-intensity chirped laser pulse to compress both longitudinally and transversely. For optimally chosen parameters, we find that the transverse and longitudinal focal lengths can be made to coincide, resulting in rapid intensity increase, ionization, and white light generation in a localized region far from the source. Coupled equations for the laser spot size and pulse duration are derived, which can describe the focusing and compression process in the low-intensity regime. More general examples involving beam focusing, compression, ionization, and white light generation near the focal region are studied by numerically solving the full set of 3D, nonlinear propagation equations.

DOI: 10.1103/PhysRevE.66.046418 PACS number(s): 52.35.Mw, 42.65.Jx, 42.65.Re, 32.80.Fb

I. INTRODUCTION

The propagation of short, intense laser pulses in the atmosphere may have a number of important applications in the areas of active and passive remote sensing, electronic countermeasures, and induced electric discharges (artificial lightning). For example, localized ultraviolet radiation generated at a remote distance by laser ionization can provide a source for active fluorescence spectroscopy of biological and chemical agents in the atmosphere. Pulses of intense, directed white light may also find applications in the areas of hyperspectral imaging and differential absorption spectroscopy.

Experiments using ultrashort ($\sim$100 fsec), high-intensity ($>10^{13}$ W/cm^2) laser pulses appear to have demonstrated long-distance atmospheric propagation, air breakdown, filamentation, and white light generation [1–14]. Intense, directed white light pulses have been generated and backscattered from atmospheric aerosols up to altitudes of $\sim$15 km [4]. The generation of pulsed THz radiation in plasma channels formed by femtosecond pulses has also been observed and analyzed [15,16]. Although many of the observations cannot be completely explained, the experimental, theoretical, and numerical results obtained to date indicate potential applications for both passive and active remote sensing [4,17,18], and induced electric discharges [10–14], among others. To achieve these potential applications it is necessary to have a comprehensive and quantitative understanding of the physical mechanisms that govern the propagation of intense, short laser pulses in air.

The propagation of intense, short laser pulses in the atmosphere involves a variety of diverse linear and nonlinear optical processes. The combined effects of diffraction, nonlinear self-focusing, ionization, and plasma defocusing play an important role in the propagation of laser and plasma filaments [1,5,6,19–26]. In addition, nonlinear bound electron effects, stimulated Raman scattering, and plasma formation contribute to considerable spectral broadening and white light generation by the laser pulse [8,9,23,27–32].

The physics governing the atmospheric propagation of short intense laser pulses can be very different from that of long laser pulses. For example, the Raman instability associated with the excitation of molecular rotational modes, which can disrupt the long-distance propagation of long (>nsec) pulses [28], may not be as disruptive for laser pulses that are shorter than the characteristic period of the rotational mode ($\sim$psec). In addition, experiments and theory indicate that the nonlinear refractive index of air is a function of the laser pulse length; e.g., for a $\sim$100-fsec pulse, it is observed that the effective nonlinear refractive index can be several times smaller than for a longer (>psec) pulse [1]. Also, because of their large spectral content, short laser pulses are more affected by dispersion. Finally, the atmospheric propagation of intense, short laser pulse trains generated by, for example, an rf linac driven free-electron laser [33], may result in sufficient spectral broadening to affect the laser absorption rate. That is, the broadened laser pulse spectrum, rather than lying between individual absorption lines, may overlap some of the lines. This could affect the thermal blooming process, which is a sensitive function of the absorption rate.

In this paper we derive, analyze, and numerically solve a system of three-dimensional (3D), nonlinear equations for atmospheric laser pulse propagation. The model includes dif-

fraction, group velocity, and higher-order dispersion, stimulated molecular Raman scattering, photoionization, nonlinear bound electron effects, ionization energy depletion, and propagation in a spatially varying atmosphere. The propagation equations are used to analyze a number of physical processes, such as optical/plasma filamentation, pulse compression, nonlinear focusing, and white light generation. A coupled set of equations for the laser power, spot size, and electron density is derived. At sufficiently low intensities where ionization is negligible, a necessary condition for equilibrium of a laser filament is derived. It is shown that at high intensities laser power depletion due to ionization implies the absence of a matched beam solution, although extended propagation is possible, provided the ionization rate is sufficiently small. For laser intensities sufficiently low that ionization effects and stimulated Raman scattering can be neglected, a set of coupled equations for the laser spot size and pulse duration are also derived. The coupled equations describe nonlinear self-focusing, compression, and spreading of chirped pulses in a spatially varying atmosphere. Simulations based on the 3D numerical solution of the general propagation equations are used to study highly nonlinear propagation in the presence of plasma generation and Raman scattering.

A process by which a laser pulse can remotely ionize a localized region of the atmosphere is studied for possible remote sensing applications. By introducing a negative frequency chirp on a relatively long laser pulse (>psec), the pulse can undergo longitudinal compression due to linear group velocity dispersion. In addition, transverse self-focusing of the pulse takes place due to atmospheric nonlinearities. For a properly chosen set of parameters, the focal distances for longitudinal compression and transverse focusing can be made to coincide, resulting in a significant intensity increase over a relatively localized region. The compressed and focused laser pulse can ionize a local region ($\sim$1 m in extent) of the atmosphere, several kilometers away from the source. The localized spark can generate ultraviolet radiation through recombination. Since many biological and chemical agents will fluoresce in the optical regime when illuminated with ultraviolet radiation, the recombination radiation can be used as a source for atmospheric fluorescence spectroscopy. For this application, the ultraviolet radiation must be generated locally since it is highly absorbed in the atmosphere.

This paper is organized as follows. In Sec. II the general nonlinear 3D propagation equations are derived. In Sec. III photoionization processes, filamentation in neutral air and white light generation (including the effects of photoionization and Raman scattering) are discussed. Using the source-dependent expansion method, coupled equations for the laser power, spot size, and electron density are derived, and an approximate equilibrium is obtained in Sec. IV. Section V presents a discussion of compression and focusing of a laser pulse in the atmosphere, leading to the generation of a spark at a remote location. Coupled equations for the laser spot size and pulse duration are derived from the propagation equations in the low-intensity regime. Using the simplified coupled equations, conditions are derived for optimal compression and focusing in the low-intensity limit. Simulations based on numerical solution of the general propagation equations on a 3D Cartesian grid are used to model high-intensity atmospheric propagation. Laser pulse propagation in a spatially varying atmosphere is also considered. Finally a summary is presented in Sec. VI. The Appendix contains the derivation of the nonlinear source terms.

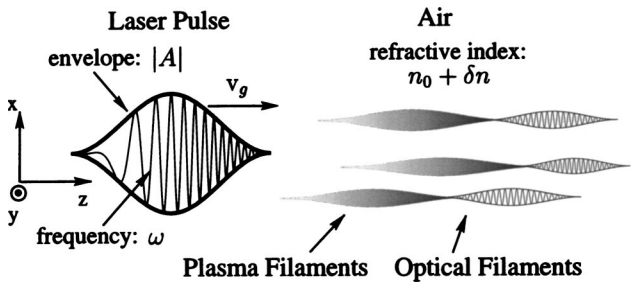

FIG. 1. Schematic illustration showing filamentation of a chirped laser pulse in air. The total nonlinear index δn, laser envelope $|A|$, and instantaneous frequency ω in the general model are assumed to be functions of the coordinates $(x,y,z,\tau=t-z/v_g)$, where v_g is the linear group velocity of the laser pulse.

II. GENERAL NONLINEAR PROPAGATION EQUATION

In this section we derive a general nonlinear 3D equation describing the propagation of an intense laser pulse in air. The equation incorporates the effects of diffraction, dispersion, ionization, pulse energy depletion due to ionization, stimulated molecular Raman scattering, nonlinearities associated with bound electrons, spatial inhomogeneity in air density, plasma wakefields, and relativistic electron motion. Figure 1 is a schematic representation illustrating the formation of optical and plasma filaments and showing the (x,y,z,τ) coordinate system used in the derivation of the propagation equations.

A. Wave equation

The starting point is the wave equation for the laser electric field $\mathbf{E}(\mathbf{r},t)$, given by

$$\left(\nabla_\perp^2+\frac{\partial^2}{\partial z^2}-\frac{1}{c^2}\frac{\partial^2}{\partial t^2}\right)\mathbf{E}=\mathbf{S}_L+\mathbf{S}_{\mathrm{NL}}, \tag{1}$$

where $\nabla_\perp^2$ is the transverse Laplacian operator and z is the coordinate in the direction of propagation. The quantities $\mathbf{S}_L$ and $\mathbf{S}_{\mathrm{NL}}$ denote source terms which are, respectively, linear and nonlinear in the laser electric field.

The laser electric field $\mathbf{E}(x,y,z,t)$, linear source term $\mathbf{S}_L(x,y,z,t)$, and nonlinear source term $\mathbf{S}_{\mathrm{NL}}(x,y,z,t)$, are written in terms of complex amplitudes $A(x,y,z,t)$, $S_L(x,y,z,t)$, and $S_{\mathrm{NL}}(x,y,z,t)$, and a rapidly varying phase $\psi(z,t)$; that is,

$$\mathbf{E}(x,y,z,t)=A(x,y,z,t)\exp[i\psi(z,t)]\hat{\mathbf{e}}_x/2+\mathrm{c.c.}, \tag{2a}$$

$$\mathbf{S}_L(x,y,z,t)=S_L(x,y,z,t)\exp[i\psi(z,t)]\hat{\mathbf{e}}_x/2+\mathrm{c.c.}, \tag{2b}$$

$$\mathbf{S}_{\mathrm{NL}}(x,y,z,t)=S_{\mathrm{NL}}(x,y,z,t)\exp[i\psi(z,t)]\hat{\mathbf{e}}_x/2+\mathrm{c.c.}, \tag{2c}$$

where $\psi(z,t)=k_0z-\omega_0t$ is the phase, k_0 is the carrier wave number, ω_0 is the carrier frequency, $\hat{\mathbf{e}}_x$ is a transverse unit vector in the direction of polarization, and c.c. denotes the complex conjugate. Substituting the field and source representations given by Eqs. (2) into Eq. (1) yields

$$\left(\nabla_\perp^2-k_0^2+\frac{\omega_0^2}{c^2}+2ik_0\frac{\partial}{\partial z}+2i\frac{\omega_0}{c}\frac{\partial}{\partial t}+\frac{\partial^2}{\partial z^2}-\frac{1}{c^2}\frac{\partial^2}{\partial t^2}\right)A(\mathbf{r},t)$$
$$=S_L(\mathbf{r},t)+S_{\mathrm{NL}}(\mathbf{r},t), \tag{3}$$

where the rapidly varying phase factor has been cancelled from both sides of the equation. Although the atmospheric density is spatially varying, the wave number is taken to be constant since the maximum change in the linear refractive index, i.e., fractional change in wave number, from sea level to vacuum is $\leqslant 10^{-4}$.

B. Linear source terms

The linear source amplitude can be expressed as [34]

$$S_L(\mathbf{r},t)=\left(\frac{\omega_0}{c}\right)^2\sum_{\ell=0}^{\infty}i^\ell\alpha_\ell(\mathbf{r})\omega_0^{-\ell}\frac{\partial^\ell A(\mathbf{r},t)}{\partial t^\ell}, \tag{4}$$

where $\ell=0,1,2,\ldots$. In terms of the conventional dispersion parameters [34], $\beta_\ell=\partial^\ell\beta(\omega)/\partial\omega^\ell|_{\omega=\omega_0}$, where $\beta(\omega)=(\omega/c)[1+4\pi\hat{\chi}_L(\omega)]^{1/2}=(\omega/c)n_0(\omega)$; the coefficients are given by

$$\alpha_\ell=-\frac{\omega_0^{\ell-2}}{\ell!}\frac{\partial^\ell}{\partial\omega_0^\ell}[c^2\beta^2(\omega_0)-\omega_0^2], \tag{5}$$

for example,

$$\alpha_1=2\left[1-\frac{c^2}{\omega_0}\beta_0\beta_1\right],\quad \alpha_2=1-c^2(\beta_1^2+\beta_0\beta_2),$$
$$\text{and}\quad \alpha_3=-c^2\omega_0\left[\beta_1\beta_2+\frac{1}{3}\beta_0\beta_3\right].$$

Here, $\hat{\chi}_L(\omega)$ is the linear susceptibility of bound electrons and $n_0(\omega)$ is the refractive index. For the cases of interest, it is sufficient to use the approximation $\beta_1\approx c^{-1}$.

C. Nonlinear source terms

The nonlinear source amplitude is due to a number of effects, and can be written as

$$S_{\mathrm{NL}}(\mathbf{r},t)=S_{\mathrm{bound}}+S_{\mathrm{Raman}}+S_{\mathrm{plasma}}+S_{\mathrm{wake}}+S_{\mathrm{rel}}+S_{\mathrm{ion}}, \tag{6}$$

where the individual contributions are derived in the Appendix. The nonlinear contribution from bound electrons, the Kerr effect, is given by

$$S_{\mathrm{bound}}(\mathbf{r},t)=\frac{\omega_0^2n_0^2n_2}{4\pi c}|A(\mathbf{r},t)|^2A(\mathbf{r},t), \tag{7}$$

where n_2 is the electronic contribution to the nonlinear refractive index. The nonlinear index defines a nonlinear self-focusing power $P_{\mathrm{NL}}=\lambda_0^2/(2\pi n_0n_2)$ (Refs. [34–37]).

The source term due to stimulated molecular Raman scattering is given by

$$S_{\mathrm{Raman}}(\mathbf{r},t)=-4\pi\frac{\omega_0^2}{c^2}\chi_LQ(t)A(\mathbf{r},t), \tag{8}$$

where χ_L is the linear susceptibility and the unitless Raman oscillator function $Q(t)$ is determined by solving Eqs. (A9) and (A10). The Raman source term can also contribute to the third-order polarization field.

The plasma source term is given by

$$S_{\mathrm{plasma}}(\mathbf{r},t)=\frac{\omega_p^2(\mathbf{r},t)}{c^2}\left(1-i\frac{\nu_e}{\omega_0}\right)A(\mathbf{r},t), \tag{9}$$

where $\omega_p(\mathbf{r},t)=[4\pi q^2n_e(\mathbf{r},t)/m]^{1/2}$ is the plasma frequency, n_e is the plasma density generated by ionization, and ν_e is the electron-neutral collision frequency. Ionization results in a plasma column that is localized to the laser axis. The plasma column causes a local decrease in the refractive index, which can defocus the laser pulse. The term proportional to the electron collision frequency is responsible for the collisional absorption of laser energy, i.e., inverse bremsstrahlung.

The source term S_{wake} is due to the possible generation of plasma waves, and is given by

$$S_{\mathrm{wake}}(\mathbf{r},t)=\frac{\omega_p^2(\mathbf{r},t)}{c^2}\frac{\delta n_e}{n_e}A(\mathbf{r},t), \tag{10}$$

where δn_e represents a plasma density perturbation driven by the ponderomotive force of the laser pulse, i.e., a plasma wakefield [38]. The density perturbation, determined by Eq. (A19) together with Gauss's equation, results in a modulation of the plasma density at the plasma frequency.

The term S_{rel} is due to relativistic effects arising from quiver motion of plasma electrons in the field of the laser, and is given by

$$S_{\mathrm{rel}}(\mathbf{r},t)=-\frac{\omega_p^2(\mathbf{r},t)}{4c^2}\left(\frac{q|A(\mathbf{r},t)|}{mc\omega_0}\right)^2A(\mathbf{r},t). \tag{11}$$

This relativistic source term defines a critical self-focusing power due to plasma [37], $P_{\mathrm{plasma}}=2c(q/r_e)^2n_0(\omega_0/\omega_p)^2$, where $r_e=q^2/mc^2$ is the classical electron radius. The total nonlinear self-focusing power consists of contributions from both P_{NL} and P_{plasma} and is given by $P_{\mathrm{NL}}P_{\mathrm{plasma}}/(P_{\mathrm{NL}}+P_{\mathrm{plasma}})$, as shown in Ref. [36]. Typically, $P_{\mathrm{plasma}}\gg P_{\mathrm{NL}}$, so that the nonlinear self-focusing power is due to bound electrons and is equal to P_{NL}.

Finally, the term describing the depletion of laser energy due to ionization is given by

$$S_{\rm ion}(\mathbf{r},t) = -8\pi i k_0 \frac{U_{\rm ion}}{c|A(\mathbf{r},t)|^2}\frac{\partial n_e}{\partial t}A(\mathbf{r},t), \qquad (12)$$

where $U_{\rm ion}$ is the characteristic ionization energy. For example, the ionization energy for O_2 is 12.1 eV while for N_2 it is 15.6 eV.

D. Full nonlinear three-dimensional propagation equation

Substituting Eqs. (4)–(12) into Eq. (3) results in the following nonlinear propagation equation for the laser envelope:

$$\begin{aligned}\Big[\nabla_\perp^2 + \Delta K^2 - \frac{\omega_p^2}{c^2}\Big(1 - i\frac{\nu_e}{\omega_0}\Big) + 2ik_0\frac{\partial}{\partial z} + \frac{\partial^2}{\partial z^2} \\ + 2i\frac{\omega_0}{c}(1-\alpha_1/2)\frac{\partial}{\partial ct} - (1-\alpha_2)\frac{\partial^2}{\partial c^2 t^2} \\ + i\alpha_3\frac{c}{\omega_0}\frac{\partial^3}{\partial c^3 t^3}\Big]A(\mathbf{r},t) \\ = -\Big(\frac{\omega_0^2 n_0^2 n_2}{4\pi c}|A|^2 + \frac{q^2}{4m^2c^4}\frac{\omega_p^2}{\omega_0^2}|A|^2 - \frac{\omega_P^2}{c^2}\frac{\delta n_e}{n_e} \\ - 8\pi i k_0 \frac{U_{\rm ion}}{|A|^2}\frac{\partial n_e}{\partial ct} + 4\pi\frac{\omega_0^2}{c^2}\chi_L Q(t)\Big)A(\mathbf{r},t), \qquad (13)\end{aligned}$$

where the summation in Eq. (4) has been limited to $\ell \leqslant 3$ and $\Delta K^2 = (1-\alpha_0)\omega_0^2/c^2 - k_0^2$.

It proves useful to transform the independent variables from z, t to z, τ, where $\tau = t - z/v_g$ and v_g will be set equal to the linear group velocity of the pulse. In terms of the new variables the derivatives transform as $\partial/\partial t \to \partial/\partial\tau$ and $\partial/\partial z \to \partial/\partial z - v_g^{-1}\partial/\partial\tau$. Under this transformation, Eq. (13) becomes

$$\begin{aligned}\Big[\nabla_\perp^2 + \Delta K^2 - \frac{\omega_p^2}{c^2}\Big(1 - i\frac{\nu_e}{\omega_0}\Big) + 2ik_0\Big(\frac{\partial}{\partial z} - \frac{2}{\beta_g}\frac{\partial^2}{\partial z\partial c\tau} + \frac{\partial^2}{\partial z^2} \\ + 2i\frac{\Delta\Omega}{c}\frac{\partial}{\partial c\tau} - (1-\beta_g^{-2}-\alpha_2)\frac{\partial^2}{\partial c^2\tau^2} \\ + i\alpha_3\frac{c}{\omega_0}\frac{\partial^3}{\partial c^3\tau^3}\Big]A(x,y,z,\tau) \\ = -\Big(\frac{\omega_0^2 n_0^2 n_2}{4\pi c}|A|^2 + \frac{q^2}{4m^2c^4}\frac{\omega_p^2}{\omega_0^2}|A|^2 - \frac{\omega_p^2}{c^2}\frac{\delta n_e}{n_e} \\ - 8\pi i k_0\frac{U_{\rm ion}}{|A|^2}\frac{\partial n_e}{\partial c\tau} + 4\pi\frac{\omega_0^2}{c^2}\chi_L Q(t)\Big)A(x,y,z,\tau), \qquad (14)\end{aligned}$$

where $\Delta\Omega = (1-\alpha_1/2)\omega_0 - \beta_g^{-1}ck_0$ and $\beta_g = v_g/c$.

The wave number k_0 and group velocity v_g appearing in Eq. (14) are as yet unspecified. It is convenient to choose them so that the form of the propagation equation is simplified. Choosing $\Delta K = 0$ and $\Delta\Omega = 0$ defines the carrier wave number and linear group velocity, respectively, as $k_0 = (1-\alpha_0)^{-1/2}\omega_0/c = n_0\omega_0/c$ and $v_g = cn_0/(1-\alpha_1) = c/(n_0 + \omega_0\partial n_0/\partial\omega_0)$. Taking $\Delta K = \Delta\Omega = 0$, the propagation equation simplifies to

$$\begin{aligned}\Big[\nabla_\perp^2 - \frac{\omega_p^2}{c^2}\Big(1 - i\frac{\nu_e}{\omega_0}\Big) + 2ik_0\frac{\partial}{\partial z} - \frac{2}{\beta_g}\frac{\partial^2}{\partial z\partial c\tau} \\ - c^2k_0\beta_2\frac{\partial^2}{\partial c^2\tau^2} + i\alpha_3\frac{c}{\omega_0}\frac{\partial^3}{\partial c^3\tau^3}\Big]A(x,y,z,\tau) \\ = -\Big(\frac{\omega_0^2 n_0^2 n_2}{4\pi c}|A|^2 + \frac{q^2}{4m^2c^4}\frac{\omega_p^2}{\omega_0^2}|A|^2 - \frac{\omega_p^2}{c^2}\frac{\delta n_e}{n_e} \\ + 8\pi i k_0\frac{U_{\rm ion}}{|A|^2}\frac{\partial n_e}{\partial c\tau} + 4\pi\frac{\omega_0^2}{c^2}\chi_L Q(t)\Big)A(x,y,z,\tau), \qquad (15)\end{aligned}$$

where a small term ($\partial^2 A/\partial z^2$) has been neglected. Equation (15) describes the 3D evolution of the complex laser field amplitude $A(x,y,z,\tau)$. The self-consistent model employed here involves the solution of Eq. (15) along with equations that describe the response of the medium (air) to the laser field. In Eq. (15), the linear dispersion response is obtained from Eq. (4), while Eq. (A6) gives the nonlinear bound electron response. The stimulated Raman response is obtained from Eqs. (A9)–(A11). Plasma effects, wakefields, and relativistic effects are given in Eq. (A20); while Eq. (A26) provides the expression for pulse energy depletion due to ionization. Finally, photoionization rates are given in the following section.

A 3D numerical simulation based on solving Eqs. (15) together with the medium response has been developed, which places the laser pulse on a Cartesian (x,y,τ) grid, allowing for the modeling of asymmetric pulse shapes and laser filamentation. The laser pulse is advanced in z according to Eq. (15) using a split-step method [34] in which the linear terms are advanced in Fourier space, while the nonlinear terms are handled in coordinate space. The equations describing ionization, wakefield generation, and Raman scattering are solved at each z step by a fourth-order Runga-Kutta integration. To facilitate computation of the plasma wakefield, the term $c^2\nabla\times\nabla\times\mathbf{E}_w$ has been neglected and the approximation $\nabla \approx \nabla_\perp - (\hat{\mathbf{e}}_z/v_g)(\partial/\partial\tau)$ has been made in Eq. (A19) and in using Gauss's equation.

III. IONIZATION, FILAMENTATION, AND WHITE LIGHT GENERATION

In the following sections we use the theoretical model presented in the previous section to analyze ionization, filamentation, and spectral broadening of short, intense laser pulses in air. The analyses of optical filament propagation and white light generation consist of substituting a self-similar form for the solution of the complex amplitude into a reduced version of Eq. (15), and obtaining equations for such quantities as the laser spot size, phase, curvature, and instantaneous frequency. While these analyses are not meant to be rigorous, they can provide some quantitative understanding of the processes considered.

A. Photoionization

The free-electron density in air can change because of ionization, recombination, and attachment processes. The rate equation for electron density n_e is

$$\frac{\partial n_e}{\partial t} = W n_n - \eta n_e - \beta_r n_e^2, \tag{16}$$

where n_n is the neutral gas density, W is the photoionization rate, η is the electron-attachment rate coefficient, and β_r is the recombination coefficient. For the laser pulses of interest here, which have durations of ~ 1 psec or less, recombination and attachment processes play a negligible role in the propagation of a single pulse [39,14].

For short laser pulses, free electrons are generated by multiphoton and tunneling processes; avalanche ionization is not significant. The principal constituents of air are nitrogen and oxygen, and hence the total photoionization rate can be written approximately as $W = 0.8 W_{N_2} + 0.2 W_{O_2}$, corresponding to the proportion of N_2 and O_2 molecules in normal atmosphere. For either one of these species, the ionization rate takes different forms according to the value of the Keldysh parameter γ_K [40], i.e.,

$$\gamma_K = 2.31 \times 10^6 \left(\frac{U_{\text{ion}}[\text{eV}]}{(\lambda^2[\mu\text{m}])(I[\text{W/cm}^2])} \right)^{1/2}, \tag{17}$$

where U_{ion} is the ionization energy. The value of the Keldysh parameter identifies the multiphoton ($\gamma_K \gg 1$) and the tunneling ($\gamma_K \ll 1$) regimes.

In the multiphoton (mp) regime, the ionization rate is [41]

$$W_{\text{mp}} = \frac{2\pi\omega_0}{(\ell-1)!} \left(\frac{I(r,z,\tau)}{I_{\text{mp}}} \right)^{\ell}, \tag{18}$$

where $I(r,z,\tau)$ is the intensity, $I_{\text{mp}} = \hbar\omega_0^2/\sigma_{\text{mp}}$, and σ_{mp} is a cross section determined empirically [25,42] to be equal to 6.4×10^{-18} cm^2 for short pulses. The characteristic multiphoton ionization intensity for a $\lambda = 1$ μm laser pulse is $I_{\text{mp}} = 5.8 \times 10^{13}$ W/cm^2. The integer ℓ denotes the minimum number of photons needed for ionization, i.e., $\ell = \text{Int}[U_{\text{ion}}/\hbar\omega_0 + 1]$.

An electron, however, can absorb more photons than is necessary for multiphoton ionization. This process is referred to as above-threshold ionization (ATI) [43]. In ATI, when the electron absorbs $s > \ell$ photons, it enters a continuum state with an excess energy of $(s-\ell)\hbar\omega_0$. This excess energy is manifested as oscillatory and ponderomotive motion of the ionized electron. For sufficiently high intensities, the coupling of these continuum states can become important. ATI was first observed by Agostini [44] who reported the occurrence of several distinct peaks in the electron energy spectrum separated from one another by the photon energy. In the traditional theoretical description, ATI is treated as a two-stage process consisting of the ionization stage and the above-threshold stage [45]. The above-threshold stage is characterized by an electron that is only weakly influenced by the atomic potential, so that its motion is dominated by the laser field. Quantum mechanical solutions of this interaction are based on Volkov states, which are the exact solutions describing a free electron (in vacuum) interacting with an oscillating electromagnetic field [46].

Although the ATI process is inherently quantum mechanical, certain aspects have classical interpretations [47]. When the number of photons per cubic wavelength is much greater than unity, the laser field can be described classically. Also, since the laser electric field is oscillatory, an electron will undergo oscillatory motion with a time-averaged kinetic energy $E_{\text{osc}} = q^2|A|^2/4m\omega_0^2$. The energy associated with the electron oscillation should be much greater than the photon energy $\hbar\omega_0$ for the classical description to apply. For the parameters of interest, i.e., $I \sim 10^{14}$ W/cm^2, $\lambda \sim 1$ μm, the number of photons in a cubic wavelength is $N_{\text{photon}} = I\lambda^3/\hbar\omega_0 c \sim 2 \times 10^{10}$ and the oscillation energy is ~ 10 eV, i.e., $\sim$eight times larger than the photon energy $\hbar\omega_0 \sim 1.2$ eV. Hence, for the parameters of interest, certain aspects of ATI can be accounted for classically, such as the enhanced energy gain of the ionized (free) electrons. Other characteristics, however, such as the quantization of the electron energy, cannot be described classically.

In our model, the energy depleted from the laser pulse due to the ATI process is accounted for classically. For example, retaining only the mixed derivative term and terms describing the linear plasma response and plasma wakefield, the propagation equation [Eq. (15)], reduces to $2ik_0(\partial A/\partial z) \approx [1 - (i/\omega_0)(\partial/\partial\tau)][(\omega_p^2/c^2)(1 + \delta n_e/n_e)A]$. The reduced propagation equation results in an equation for energy conservation given by $\partial(|A|^2/8\pi)/\partial z = -N_e(\partial E_{\text{osc}}/\partial c\tau) - 2E_{\text{osc}}(\partial N_e/\partial c\tau)$, where $N_e = n_e + \delta n_e$. The first term on the right-hand side accounts for laser energy that is converted to electron oscillatory motion. This term indicates that laser energy is converted to electron kinetic energy at the front of the pulse, while at the back of the pulse the oscillatory kinetic energy is converted back to laser energy. The second term on the right-hand side, in the absence of ionization, accounts for the energy lost due to the ponderomotive excitation of plasma wakefields.

In the tunneling regime, the time-averaged ionization rate for a linearly polarized laser pulse is [40]

$$W_{\text{tun}} = 4\alpha_{\text{tun}}\Omega_0 \left(\frac{U_{\text{ion}}}{U_H} \right)^{7/4} \left(\frac{I_H}{I} \right)^{1/4} \exp\left[-\frac{2}{3} \left(\frac{U_{\text{ion}}}{U_H} \right)^{3/2} \left(\frac{I_H}{I} \right)^{1/2} \right], \tag{19}$$

where $\Omega_0 = 4.1 \times 10^{16}$ sec^{-1} is the fundamental atomic frequency, $I_H = 3.6 \times 10^{16}$ W/cm^2, and $U_H = 13.6$ eV is the ionization energy of hydrogen. Finally, since the peak laser intensity in a guided filament is typically $\sim 10^{13}$ W/cm^2, the ionization process is neither purely multiphoton ($I < 10^{12}$ W/cm^2) nor tunneling ($I > 10^{14}$ W/cm^2). In the intermediate ($\gamma_K \sim 1$) regime, an analytical fit is employed, having the form $W_x = \alpha_x I^{[\kappa_1 + \kappa_2 \ln(I)]}$. In the expressions for the ionization rates, α_{tun}, σ_{mp}, α_x, κ_1, and κ_2 are fitting constants chosen to match the experimental measurements. As an example, Fig. 2 is a plot of the ionization rate versus intensity for a laser wavelength of 0.8 μm. The fitting con-

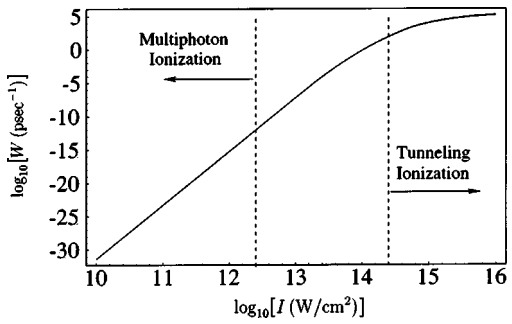

FIG. 2. Dependence of ionization rate on laser intensity. Dashed lines delineate approximate tunneling ($\gamma_K<0.5$) and multiphoton ($\gamma_K>5$) ionization regimes.

stants for this plot are chosen to reproduce the experimentally measured short-pulse ionization rate reported in Refs. [25] and [42].

B. Filamentation in neutral air

Perturbations or hot spots on the intensity profile of a laser beam can grow as a result of a filamentation instability. Filamentation, i.e., transverse breakup, of a laser beam is due to the interplay between diffraction and nonlinear self-focusing. Consider a laser beam propagating in a neutral gas, for which the nonlinear focusing power is $P_{\rm NL}$ and the transverse laser intensity profile is slightly perturbed by a small, localized hot spot. The spatial growth rate of this perturbation due to the filamentation instability [37,48] is given by

$$\Gamma=\frac{\lambda}{\pi x_\perp}\left(\frac{3\pi I}{P_{\rm NL}}-\frac{1}{x_\perp^2}\right)^{1/2}, \tag{20}$$

where I is the laser intensity and $x_\perp$ is the characteristic transverse dimension of the filament, i.e., spot size. As a function of the dimension of the filament, the growth rate vanishes for $x_\perp\leqslant x_{\rm min}\equiv[P_{\rm NL}/(3\pi I)]^{1/2}$, reaches a maximum equal to $\Gamma_{\rm max}=3\lambda I/(2P_{\rm NL})$ at $x_\perp=\sqrt{2}x_{\rm min}$, and decreases inversely with $x_\perp$ as $x_\perp\to\infty$. At maximum growth rate the power within the filament is roughly equal to $P_{\rm NL}$. It is therefore expected that a laser beam with a power P will break up into N filaments where $N\leqslant P/P_{\rm NL}$. As an example, the nonlinear focusing power associated with air for a 1-μm wavelength, ~1-nsec-duration laser is in the range of ~3 GW ($n_2\sim5.6\times10^{-19}$ cm^2/W) [49]; therefore a 100-GW laser pulse may eventually breakup into a few tens of filaments.

C. White light generation

The nonlinear interaction of an intense, short laser pulse in the atmosphere can result in significant spectral broadening due to self phase modulation. The phase of the laser field becomes modulated through the time-dependent refractive index by nonlinear effects, ionization, Raman processes, etc. Although 3D effects also play an important role in spectral broadening, a 1D analysis is useful. The solution of the laser pulse propagation equation in 1D has the form $A(z,\tau)=B(z,\tau)\exp[i\theta(z,\tau)]$, where the amplitude B and phase θ are real functions of z and τ. The instantaneous frequency of the pulse on axis can be defined as

$$\omega(z,\tau)=\omega_0-\frac{\partial\theta(z,\tau)}{\partial\tau}. \tag{21}$$

To determine $\partial\theta/\partial\tau$ we rewrite the full nonlinear propagation equation in Eq. (15) in the form

$$2ik_0\frac{\partial A}{\partial z}=-[n^2(z,\tau)-n_0^2]\frac{\omega_0^2}{c^2}A, \tag{22}$$

where $n(z,\tau)$ is the index of refraction in configuration space variables. For the present purposes, only the terms contributing to the index of refraction from bound electrons [Eq. (7)], Raman scattering [Eq. (8)], and the plasma [Eq. (9)] will be retained. The bound electron and Raman contributions are given in Eq. (A15) while the plasma contribution to the index is $-\omega_p^2(z,\tau)/2n_0\omega_0^2$. The nonlinear index can be written as

$$\delta n=n(z,\tau)-n_0=\delta n_{\rm bound}+\delta n_{\rm Raman}+\delta n_{\rm plasms},$$

that is,

$$\delta n(\mathbf{r},\tau)=n_2I(\mathbf{r},\tau)-n_R\int_{-\infty}^{\tau}d\tau'\,W(\tau')R(\tau-\tau')I(\mathbf{r},\tau')$$
$$-\omega_p^2(z,\tau)/2n_0\omega_0^2, \tag{23}$$

where n_R is the Raman contribution to the nonlinear index for long pulses, $W(\tau)$ is the population inversion variable, and

$$R(\tau)=\left(\frac{\omega_R^2+\Gamma_2^2}{\omega_R}\right)e^{-\Gamma_2\tau}\sin(\omega_R\tau) \tag{24}$$

is the Green's function for the Raman process normalized such that $\int_0^\infty d\tau R(\tau)=1$, ω_R is the characteristic Raman frequency, and Γ_2 is a phenomenological damping rate (see the Appendix for the details). In the remainder of the paper we will assume negligible population inversion, $W(\tau)\approx-1$. To obtain the instantaneous frequency along the pulse, we substitute the representation of the complex amplitude A into Eq. (22), with the result

$$\frac{\partial\theta}{\partial z}\approx\frac{\omega_0}{c}\,\delta n_r(z,\tau), \tag{25a}$$

$$\frac{\partial\ln(B)}{\partial z}\approx-\frac{\omega_0}{c}\,\delta n_i(z,\tau), \tag{25b}$$

where $\delta n_r(\delta n_i)$ is the real (imaginary) part of δn, which is assumed small compared to unity. The instantaneous frequency spread along the pulse is given by Eq. (21), together with Eq. (25a),

$$\delta\omega(z,\tau)=\omega(z,\tau)-\omega_0=-\frac{\omega_0}{c}\int_0^z\frac{\partial\delta n_r(z',\tau)}{\partial\tau}dz'. \tag{26}$$

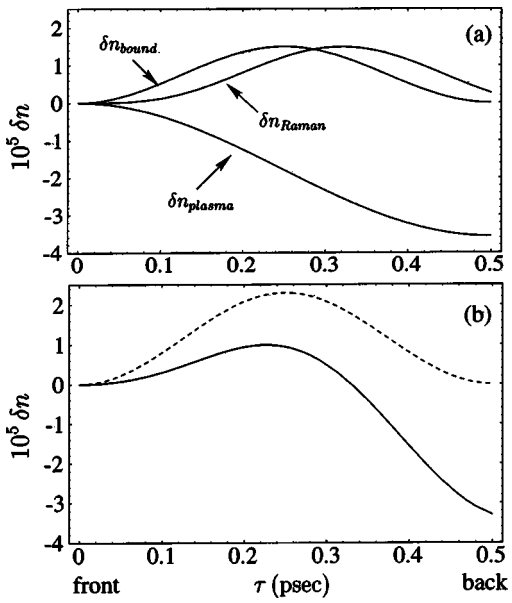

FIG. 3. (a) Variations of the nonlinear refractive index due to bound electrons, Raman effects, and plasma generation, as given by Eq. (23) versus pulse time $\tau = t - z/v_g$, for a laser pulse with wavelength $\lambda = 0.775\ \mu$m, peak intensity $I_0 = 5\times 10^{13}$ W/cm^2, and pulse duration $\tau_L = 500$ fs. (b) Total nonlinear refractive index (solid curve), i.e., $\delta n_{\rm bound} + \delta n_{\rm Raman} + \delta n_{\rm plasma}$, and laser intensity (dashed curve) versus τ.

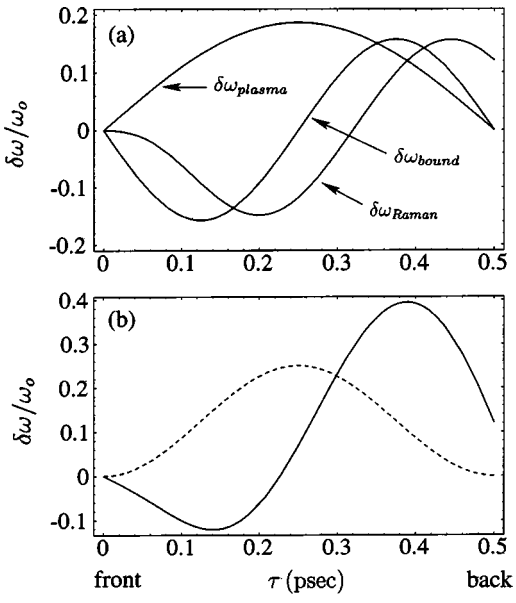

FIG. 4. (a) Instantaneous frequency shift, Eq. (27), due to bound electrons, Raman effects, and plasma versus pulse time $\tau = t - z/v_g$ after propagating 0.5 m in air. A laser pulse with wavelength $\lambda = 0.775\ \mu$m, peak intensity $I_0 = 5\times 10^{13}$ W/cm^2, and pulse duration $\tau_L = 500$ fs is assumed. (b) Total frequency shift (solid curve), i.e., $\delta\omega_{\rm bound} + \delta\omega_{\rm Raman} + \delta\omega_{\rm plasma}$ and laser intensity (dashed curve) versus τ.

Note that only the nonlinear terms in the refractive index will create new frequencies and the linear terms redistribute the frequencies within the pulse. The instantaneous frequency spread is $\delta\omega = \delta\omega_{\rm bound} + \delta\omega_{\rm Raman} + \delta\omega_{\rm plasma}$, that is,

$$\delta\omega(z,\tau) = \left(-n_2 \frac{\partial I}{\partial \tau} + n_R \int_0^\tau d\tau' W(\tau') \frac{\partial R(\tau - \tau')}{\partial \tau} I(\mathbf{r}, \tau') + \frac{1}{2 n_0 \omega_0^2} \frac{\partial \omega_p^2}{\partial \tau} \right) \frac{\omega_0 z}{c}, \tag{27}$$

where $I = c n_0 B^2 / 8\pi$ is the intensity.

As an example, consider a laser pulse with wavelength $\lambda = 0.775\ \mu$m, amplitude $A(z,\tau) = \sqrt{8\pi I_0 / c}\,\sin(\pi\tau/\tau_L)$ for $0 \leqslant \tau \leqslant \tau_L$ (and zero otherwise), peak intensity $I_0 = 5 \times 10^{13}$ W/cm^2, and pulse duration $\tau_L = 500$ fsec propagating in air. For the short-pulse regime, the bound electron and Raman effects are assumed to have the numerical values $n_2 = n_R = 3\times 10^{-19}$ cm^2/W, $\omega_R = 1.6\times 10^{13}$ sec^{-1}, and $\Gamma_2 = 1.3\times 10^{13}$ sec^{-1} [50]. For the plasma term, the dominant ionization mechanism is taken to be multiphoton ionization of O_2, so that the ionization rate is given by Eq. (18), with $\ell = 8$, for $\lambda = 0.775\ \mu$m.

For these parameters, Fig. 3(a) plots the individual contributions to δn, given by Eq. (23), due to bound electrons, Raman scattering, and plasma. Bound electron effects produce an increase in the refractive index that is proportional to the laser intensity, while the generation of plasma causes the refractive index to decrease from the front of the pulse to the back. The Raman response causes an increase in the refractive index at the front and peak of the pulse and a decrease at the back. The sum of the individual contributions to the refractive index, plotted in Fig. 3(b), shows that for these parameters, the variation of the refractive index is of the order 10^{-5}.

Figure 4(a) plots the normalized instantaneous frequency shifts due to bound electrons, stimulated Raman scattering, and plasma after propagating for 50 cm in air. For these parameters the variation in the frequency shifts due to the various effects are comparable in magnitude. The bound electrons produce a redshift at the front of the pulse and a blue shift at the back, while ionization produces a blue shift across the entire pulse. Stimulated Raman scattering produces a red shift near the front of the pulse and a blue shift at the back. The net frequency shift, i.e., the sum of the bound electron, plasma, and Raman contributions, plotted in Fig. 4(b), shows a 10% redshift at the front of the pulse and a larger 40% blue shift at the back.

IV. SELF-GUIDED PROPAGATION OF AN IONIZING LASER PULSE

In this section, long-range propagation of an ionizing laser filament in air is considered. The propagation distance of a laser pulse in air is limited by a number of processes. Two fundamental laser pulse propagation mechanisms that can, in principle, result in extended propagation distances are (i) moving foci and (ii) self-guiding. In the moving foci mechanism the focal length depends on laser power through the optical Kerr effect, and different temporal slices of the laser pulse focus at different distances [51,52]. This can give the illusion of extended propagation. However, only an infini-

tesimal fraction of the laser energy is propagated over extended distances. In the self-guiding mechanism, extended propagation distances can be obtained by balancing the defocusing effects of diffraction and plasma formation against nonlinear atomic focusing, i.e., Kerr effect. In self-guiding, losses such as ionization can deplete the laser pulse energy and significantly limit the propagation distance, as shown below.

The process of ionization and optical filament propagation can be analyzed by retaining diffraction, the nonlinear refractive index, plasma effects, and laser pulse energy depletion due to ionization in Eq. (15), i.e.,

$$\left(\nabla_\perp^2+2ik_0\frac{\partial}{\partial z}+\gamma|A(r,z,\tau)|^2-\frac{\omega_p^2(z,\tau)}{c^2}+\frac{8\pi ik_0}{c}\frac{U_{\rm ion}}{|A|^2}\frac{\partial n_e}{\partial\tau}\right)A(r,z,\tau)=0, \tag{28}$$

where $\gamma=\omega_0^2n_0^2n_2/4\pi c$.

A. Source-dependent expansion method

The following analysis of Eq. (28) is based on the source-dependent expansion (SDE) method that was originally developed in Ref. [53]. In the SDE formulation, a reduced wave equation of the general form

$$\left(\nabla_\perp^2+2ik_0\frac{\partial}{\partial z}\right)A(r,z,\tau)=M(r,z,\tau)A(r,z,\tau) \tag{29}$$

is solved by a variation of parameter technique where $M(r,z,\tau)$ is a known nonlinear function of $A(r,z,\tau)$. The complex electric field amplitude is given by

$$A(r,z,\tau)=B(z,\tau)\exp[i\theta(z,\tau)]\times\exp\{-[1+i\alpha(z,\tau)]r^2/R^2(z,\tau)\}, \tag{30}$$

where B is the field amplitude, θ is the phase, R is the spot size, and α is related to the curvature of the wave front. The quantities B, θ, R, and α are real functions of z and τ. Using the SDE method, a set of self-consistent coupled equations for the pulse amplitude $B(z,\tau)$, phase $\theta(z,\tau)$, curvature $\alpha(z,\tau)$, and spot size $R(z,\tau)$, can be derived. Applying the SDE method, we find

$$\frac{1}{BR}\frac{\partial(BR)}{\partial z}=F_i, \tag{31a}$$

$$\frac{\partial\theta}{\partial z}+\frac{(1+\alpha^2)}{k_0R^2}+\frac{\alpha}{R}\frac{\partial R}{\partial z}-\frac{1}{2}\frac{\partial\alpha}{\partial z}=-F_r, \tag{31b}$$

$$\frac{1}{R}\frac{\partial R}{\partial z}+\frac{2\alpha}{k_0R^2}=-G_i, \tag{31c}$$

$$\frac{1}{2}\frac{\partial\alpha}{\partial z}+\frac{(1+\alpha^2)}{k_0R^2}=-G_r-\alpha G_i, \tag{31d}$$

where the subscripts (r, i) denote the real and imaginary parts of the function, respectively. The details of a related derivation using the SDE method can be found in Ref. [54]. The complex functions F and G used in Eqs. (31) are given by

$$F(z,\tau)=\frac{1}{2k_0}\int_0^\infty d(2r^2/R^2)M(r,z,\tau)\exp(-2r^2/R^2), \tag{32a}$$

$$G(z,\tau)=\frac{1}{2k_0}\int_0^\infty d(2r^2/R^2)M(r,z,\tau)(1-2r^2/R^2)\times\exp(-2r^2/R^2). \tag{32b}$$

Equations (31) can be combined to give an equation for the pulse power and spot size,

$$\frac{1}{P}\frac{\partial P}{\partial z}=2F_i, \tag{33a}$$

$$\frac{\partial^2R}{\partial z^2}-\frac{4}{k_0^2R^3}(1+k_0R^2G_r)+\left(2\frac{\partial R}{\partial z}+RG_i\right)G_i+R\frac{\partial G_i}{\partial z}=0, \tag{33b}$$

where $P(z,\tau)=cR^2B^2/16$ is the laser power. For the present problem, we find from Eq. (28) that

$$M(r,z,\tau)=-\gamma|A(r,z,\tau)|^2+\frac{\omega_p^2(r,z,\tau)}{c^2}-\frac{8\pi ik_0}{c}\frac{U_{\rm ion}}{|A|^2}\frac{\partial n_e(r,z,\tau)}{\partial\tau}. \tag{34}$$

Since the multiphoton ionization rate is proportional to the laser intensity to the power of ℓ, Eqs. (16) and (18) indicate that the radial dependence of the plasma density is given by $n_e(r,z,\tau)=n_{e0}(z,\tau)\exp(-2\ell r^2/R^2)$. Substituting Eq. (34) into Eqs. (32) gives

$$F(z,\tau)=\frac{1}{2k_0}\left(-\frac{\gamma}{2}B^2+\frac{1}{\ell+1}\frac{\omega_{p0}^2}{c^2}-i\frac{8\pi k_0}{c}\frac{1}{\ell}\frac{U_{\rm ion}}{B^2}\frac{\partial n_{e0}}{\partial\tau}\right), \tag{35a}$$

$$G(z,\tau)=\frac{1}{2k_0}\left(-\frac{\gamma}{4}B^2+\frac{\ell}{(\ell+1)^2}\frac{\omega_{p0}^2}{c^2}-i\frac{8\pi k_0}{c}\frac{(\ell-1)}{\ell^2}\frac{U_{\rm ion}}{B^2}\frac{\partial n_{e0}}{\partial\tau}\right). \tag{35b}$$

Finally, substituting Eqs. (35) into Eqs. (33), the laser pulse power and spot size are found to be given by

$$\frac{\partial P}{\partial z}=-\frac{\pi}{2}U_{\rm ion}\frac{R^2}{\ell}\frac{\partial n_{e0}}{\partial\tau} \tag{36a}$$

and

$$\frac{\partial^2 R}{\partial z^2} - \frac{4}{k_0^2 R^3}\left(1 - \frac{P}{P_{\rm NL}} + \frac{2\pi\ell}{(\ell+1)^2} r_e R^2 n_{e0}\right) = -\frac{(\ell-1)}{2\ell}\frac{1}{R^3}\left\{R^2\frac{\partial}{\partial z}\left(\frac{R^2}{P}\frac{\partial P}{\partial z}\right) + \frac{(\ell-1)}{2\ell}\left(\frac{R^2}{P}\frac{\partial P}{\partial z}\right)^2\right\}, \tag{36b}$$

where $P_{\rm NL} = c/2\gamma = \lambda^2/(2\pi n_2)$ is the nonlinear focusing power, ℓ is the number for photons needed for multiphoton ionization, $U_{\rm ion}$ is the ionization energy, $n_{e0}(z,\tau)$ is the electron density on axis generated by photoionization, the linear index has been set equal to unity ($n_0 = 1$), and $r_e = q^2/mc^2 = 2.8\times 10^{-13}$ cm is the classical electron radius. Note that the $1/\ell$ dependence of the power loss in Eq. (36a) is due to the fact that the radius of the plasma channel is $R/\sqrt{2\ell}$ for multiphoton ionization. The $1/\ell$ dependence of Eq. (36a) is also apparent from energy conservation considerations. The energy lost by the laser pulse due to multiphoton ionization in propagating a distance Δz is given approximately by $\Delta W = (n_{e0}\Delta z \pi R^2/2\ell)U_1$, and taking a derivative with respect to time leads to Eq. (36a).

The on-axis electron density generated by multiphoton ionization is given by Eq. (25) (evaluated at $r = 0$),

$$\frac{\partial n_{e0}}{\partial \tau} = W_{\rm mp}(r=0) n_n = \frac{2\pi\omega_0}{(\ell-1)!}\left(\frac{I}{I_{\rm mp}}\right)^{\ell} n_n, \tag{37}$$

where $I(z,\tau) = 2P/(\pi R^2)$ is the intensity on axis. Equation (36a) indicates that the laser power decreases as a function of propagation distance in the presence of ionization since energy is expended in ionizing the air. The quantity on the right-hand side of the equation for the spot size, Eq. (36b), represents the effects of energy loss due to ionization and indicates that a matched, self-guided filament, is not possible. The single-photon ionization case ($\ell = 1$) is a special situation. The right-hand side of Eq. (36b) vanishes, since the ionization term in Eq. (28) is independent of r for $\ell = 1$, and the ionization process does not affect the focusing properties of the pulse.

B. Self-guiding condition

An approximate equilibrium of the filament's spot size can be found when the energy depletion due to ionization is low. Neglecting ionization on the right-hand side of Eq. (36b) and taking $\partial R/\partial z = 0$ gives an approximate equilibrium condition in terms of the filament power, spot size, and on-axis electron density,

$$P_{\rm eq}(\tau) = P_{\rm NL}\left(1 + \frac{2\pi\ell}{(\ell+1)^2} r_e R_{\rm eq}^2(\tau) n_{e0}(\tau)\right), \tag{38}$$

where the subscript eq denotes the equilibrium value. The electron density dependence can be removed by differentiating Eq. (38) with respect to τ and using Eq. (37). The resulting equilibrium condition is in terms of a differential equation

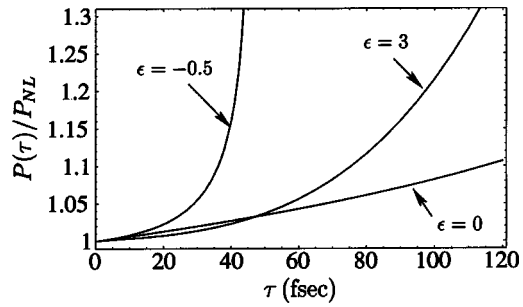

FIG. 5. Dependence of normalized laser power on pulse time $\tau = t - z/v_g$, for the equilibrium described by Eq. (39). The spot size variation is assumed to have the form $R(\tau)/R_{\rm eq} = 1 + \epsilon\tau/\tau_R$, with $\tau_R = 120$ fsec and $R_{\rm eq} = 50$ μm. The laser pulse has wavelength $\lambda = 0.775$ μm. Multiphoton ionization of O_2 ($\ell = 8$ for $\lambda = 0.775$ μm) and $P_{\rm NL} = 1.7$ GW are assumed.

$$\frac{\partial}{\partial\tau}\left(\frac{\tilde{P}(\tau)-1}{\tilde{R}^2(\tau)}\right) = \Omega_{\rm ion}\frac{\tilde{P}^{\ell}(\tau)}{\tilde{R}(\tau)^{2\ell}}, \tag{39}$$

where $\tilde{P}(\tau) = P_{\rm eq}(\tau)/P_{\rm NL}$, $\tilde{R}(\tau) = R_{\rm eq}(\tau)/R_{\rm eq}(0)$, and

$$\Omega_{\rm ion} = \frac{\pi}{(\ell+1)^2}\frac{\ell}{(\ell-1)!}\frac{\omega_n^2}{c^2}R_{\rm eq}^2(0)\left(\frac{P_{\rm NL}}{\pi R_{\rm eq}^2(0) I_{\rm mp}/2}\right)^{\ell}\omega_0, \tag{40}$$

where $\omega_n = (4\pi q^2 n_n/m)^{1/2}$. Since there is no plasma at the head of the pulse to counteract self-focusing, the initial condition on the power is $\tilde{P}(0) = 1$. Consider a particular set of examples for which the spot size is taken to vary linearly from the front of the pulse to the back, i.e., $\tilde{R}(\tau) = 1 + \varepsilon\tau/\tau_R$. Figure 5 plots solutions of Eq. (39), i.e., power versus τ for several values of ε corresponding to cases in which the spot size is increasing, constant or decreasing with τ. The laser wavelength is taken to be $\lambda = 0.775$ μm, $P_{\rm NL} = 1.7$ GW, and multiphoton ionization of O_2 is assumed, i.e., $\ell = 8$. To counteract plasma defocusing, the laser power must increase with τ to maintain equilibrium. For these parameters, the variation of the power along the pulse is the smallest for the constant spot size example.

C. Pulse energy depletion due to ionization and maximum propagation distance

The rate of change of laser pulse energy can be found by integrating Eq. (36a) over the pulse length,

$$\frac{\partial E_{\rm pulse}}{\partial z} = -\frac{\pi}{2}\frac{U_{\rm ion}}{\ell}\int_0^{\tau_L} d\tau R^2 \frac{\partial n_{e0}}{\partial\tau}, \tag{41}$$

where $E_{\rm pulse}(z) = \int_0^{\tau_L} d\tau P(z,\tau)$ is the pulse energy and τ_L is the pulse duration. Equation (41) can be approximately evaluated by taking the laser spot size to be nearly constant, i.e., independent of τ, and using the approximate equilibrium condition in Eq. (38),

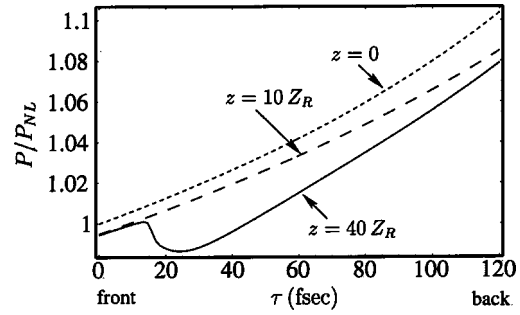

FIG. 6. Solutions of the power and spot size equations, Eqs. (36), showing power profiles versus pulse time $\tau=t-z/v_g$ at different propagation distances. The power profile at $z=0$ is an equilibrium described by Eq. (38). For the initial laser pulse, $\lambda=0.775\ \mu$m, $I_0(\tau=0)=4.3\times10^{13}$ W/cm^2, $T_0=120$ fsec, $R_0(\tau)=50\ \mu$m, i.e., an initially uniform spot size, and Rayleigh length $Z_R=\pi R_0^2/\lambda=1$ cm. Multiphoton ionization of O_2 ($\ell=8$ for $\lambda=0.775\ \mu$m) and $P_{\rm NL}=1.7$ GW are assumed.

$$\frac{\partial E_{\rm pulse}}{\partial z}\approx-\frac{U_{\rm ion}}{4r_e}\frac{(\ell+1)^2}{\ell^2}\left(\frac{P(\tau_L)}{P_{\rm NL}}-1\right). \tag{42}$$

The energy loss rate is independent of the number of photons needed to ionize the air molecules when ℓ is large. The maximum distance a pulse can propagate ($L_{\rm max}$) can be estimated by assuming that all the pulse energy goes into ionizing the air,

$$L_{\rm max}\sim\frac{4r_e}{U_{\rm ion}}\frac{\ell^2}{(\ell+1)^2}\frac{E_{\rm pulse}(0)}{(P/P_{\rm NL}-1)}, \tag{43}$$

where $E_{\rm pulse}(0)$ is the initial laser pulse energy. In principle, extended propagation or self-guiding is possible only when the laser pulse power is approximately equal to (but slightly greater than) the nonlinear focusing power, which (for air) is $P_{\rm NL}\approx2$ GW.

D. Propagation of an ionizing laser pulse

Equations (36) are solved numerically to illustrate an example of high-intensity pulse propagation in air. We consider a laser pulse with wavelength $\lambda=0.775\ \mu$m and a uniform initial spot size $R_0=50\ \mu$m, which corresponds to a Rayleigh length of $Z_R=\pi R_0^2/\lambda\approx1$ cm. The initial intensity at the front of the pulse is $I_0(\tau=0)=4.3\times10^{13}$ W/cm^2. In calculating the ionization rate, we assume multiphoton ionization of O_2 so that $\ell=8$, $\lambda=0.775\ \mu$m, and $U_{\rm ion}=12.1$ eV. The initial power profile is chosen to correspond to an equilibrium given by Eq. (38). The equilibrium power profile is perturbed by a 0.1% amplitude modulation, and its evolution shown in Fig. 6. For the first ten Rayleigh lengths, power is depleted uniformly throughout the pulse by ionization. As the back of the pulse is defocused by the presence of plasma, the intensity drops and ionization ceases. The front of the pulse remains focused and continues to ionize and lose energy. This leads to a localized depletion of power at the head of the pulse, which is evident in the power profile at $z=40Z_R$. For $z>40Z_R$, the pulse intensity decreases to a level where energy losses and defocusing due to ionization become negligible. The result is that the power profile remains relatively unchanged for $z>40Z_R$. The spot size and intensity, however, continue to evolve.

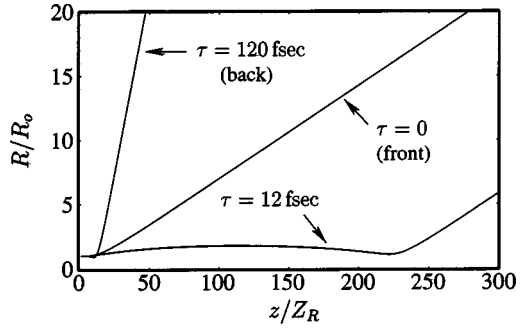

FIG. 7. Normalized spot size versus propagation distance at three different times within the pulse ($\tau=0$, 12, 120 fsec), for the same parameters as in Fig. 6. The portion of the pulse around $\tau=12$ fsec maintains a relatively constant spot size for over 200 Rayleigh lengths.

Figure 7 shows the evolution of the laser spot size at three different locations within the pulse, i.e., the front ($\tau=0$), within the body of the pulse ($\tau=12$ fsec), and at the back ($\tau=120$ fsec). The spot size remains relatively constant throughout the pulse for the first ten Rayleigh lengths of propagation before the equilibrium is lost. At $z=10Z_R$, the front and back of the pulse start to diffract. The spot size at the back increases at a faster rate due to the initial defocusing caused by the plasma. However, the portion of the pulse around $\tau=12$ fsec maintains at a constant spot size for over 200 Rayleigh lengths before diffracting.

Figure 8 shows a shaded contour plot of the on-axis laser intensity as a function of τ and z. The initial laser pulse at $z=0$ spans the length of the plot. The defocusing of the front and back leads the formation of a very short pulse (~5 fsec) in the first ~80 Rayleigh lengths of propagation. However, other mechanisms that are not included in the reduced SDE

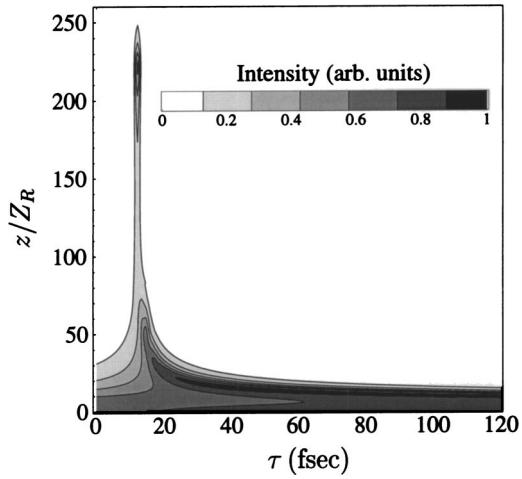

FIG. 8. Level plot of intensity versus pulse time $\tau=t-z/v_g$ and normalized propagation distance z/Z_R for the laser pulse of Figs. 6 and 7. A very short pulse of length ≈5 fsec with power $P\approx P_{\rm NL}$ is generated at $z\approx80Z_R$, and propagates for $\approx150Z_R$ before diffracting.

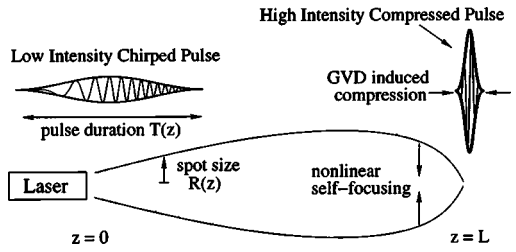

FIG. 9. Schematic illustration of the simultaneous transverse and longitudinal compression of a chirped laser pulse due to nonlinear self-focusing and group velocity dispersion in air.

equations, e.g., group velocity dispersion, will affect the propagation of such short pulses. This short pulse, which is characterized by $P \sim P_{\mathrm{NL}}$, propagates for an additional $150 Z_R$ before diffracting. This short pulse generation process resembles the relativistic guiding and pulse shortening schemes proposed in earlier works [55,56], except that here ionization contributes to the defocusing, and guiding is accomplished through the Kerr effect associated with bound electrons.

V. COMPRESSION AND FOCUSING OF LASER PULSES IN AIR

In this section the theoretical model together with simulations are used to study longitudinal and transverse compression and ionization of chirped laser pulses in the atmosphere. A low-intensity chirped laser pulse propagating in air can compress longitudinally due to linear group velocity dispersion and focus transversely due to nonlinear effects. For optimally chosen parameters, the longitudinal, transverse, and focal distances can be made to coincide, resulting in a rapid intensity increase and ionization near the focal region. This scheme for remote ionization is illustrated schematically in Fig. 9.

The propagation of the high-intensity laser pulse near the focal region is markedly different from its propagation far from focus, where the intensity is low. In the following subsections we consider separately the low-intensity propagation regime, where ionization and Raman processes are not important, and the propagation near focus, where the laser intensity becomes so sufficiently high that ionization occurs. In the low-intensity regime, a coupled set of equations for the laser spot size and pulse length are derived. Numerical solutions of the coupled equations are compared with the full numerical 3D simulation in the low-intensity regime. Propagation near focus, in the high-intensity regime, is examined using the full 3D numerical simulations.

The simulations model the propagation of $\sim$100-fsec pulses with $\lambda = 0.775\ \mu$m and intensities as large as $\sim 10^{13}$ W/cm^2. The dominant plasma generation mechanism is the multiphoton ionization of O_2, which although less abundant than N_2, has a lower ionization energy. The ionization rate given by Eq. (18) with $\ell = 8$ agrees well with the ionization rate plotted in Fig. 2 over the intensity range of 10^{12}–10^{14} W/cm^2. The parameters used in modeling the rotational Raman response are the short-pulse parameters given in the Appendix, i.e., rotational frequency $\omega_R = 16 \times 10^{12}$ sec^{-1}, damping rate $\Gamma_2 = 1.3 \times 10^{13}$ sec^{-1}, and $n_R \approx n_2 = 3 \times 10^{-19}$ cm^2/W. The group velocity dispersion (GVD) parameter is $\beta_2 = 2.2 \times 10^{-31}$ sec^2/cm, and higher-order dispersion has been neglected. For the range of intensities and pulse durations examined, the effects of collisional ionization, recombination, and plasma wakefields are not important and have also been neglected. For a typical plasma density of 10^{16} cm^{-3}, peak intensity $I \sim 10^{14}$ W/cm^2, pulse duration $\tau_L \sim 100$ fsec, and laser wavelength $\lambda = 0.775\ \mu$m, the ratio of the pulse duration to the plasma period is $\omega_p \tau_L / 2\pi \sim 0.1$; and the density perturbation associated with the wakefield is of the order $\delta n_e / n_e \sim 10^{-5}$. A brief discussion of the numerical methods used in the simulation is found at the end of Sec. II.

A. Low-intensity propagation regime

If the laser intensity is sufficiently low, the effects of ionization and Raman scattering will not be important and the propagation equation in a spatially varying atmospheric density, i.e., Eq. (15), reduces to

$$\left[\nabla_\perp^2 + 2ik_0 \frac{\partial}{\partial z} - c^2 k_0 \beta_2(z) \frac{\partial^2}{\partial c^2 \tau^2} + \gamma(z) |A(r,z,\tau)|^2 \right] A(r,z,\tau) = 0. \tag{44}$$

In writing Eq. (44), higher-order dispersion has been neglected. The spatial variation of the atmosphere is taken into account mainly through the z dependence of the group velocity dispersion coefficient $\beta_2(z)$ and the nonlinear refractive index $n_2(z)$, both of which are proportional to the neutral density. In principle, the wave number k_0 is also dependent on the neutral density, but is taken to be constant since the fractional change in k_0 is less than $\sim 10^{-4}$, as noted in the discussion of Eq. (3).

Equation (44) can be solved numerically; however, a significant simplification of the equation is possible by assuming that the evolution of the laser pulse is self-similar. That is, we assume that the pulse is described by an analytical form that depends on certain spatially dependent parameters, such as the spot size and pulse duration of the laser pulse. With this assumption, a set of simplified coupled equations can be derived for the evolution of the spot size, pulse duration, amplitude, and phase of the laser field. Assuming that the laser pulse has a Gaussian shape in both the transverse and longitudinal directions, the complex amplitude can be written as

$$A(r,z,\tau) = B(z) e^{i\theta(z)} e^{-[1+i\alpha(z)] r^2/R^2(z)} e^{-[1+i\beta(z)]\tau^2/T^2(z)}, \tag{45}$$

where B is the field amplitude, θ is the phase, R is the spot size, α is related to the curvature of the wave front, T is the laser pulse duration, and β is the chirp parameter. The quantities B, θ, T, R, α, β are real and functions of the propagation distance z. The instantaneous frequency spread along the pulse, i.e., chirp, is $\delta\omega(z,\tau) = 2\beta(z)\tau / T^2(z)$, where $\beta < 0$ (> 0) results in a negative (positive) frequency chirp, i.e., frequency decreases (increases) towards the back of the

pulse. The full frequency chip along the pulse from front to back, i.e., from $\tau=-T$ to T, is $\delta\omega_{\rm full}=4\beta/T$.

Substituting Eq. (45) into Eq. (44), one obtains an identity in the variables r and τ. Equating the like powers of r and τ, the following coupled equations for R and T are obtained:

$$\frac{\partial^2 R}{\partial z^2}=\frac{4}{k_0^2R^3}\left(1-\frac{E_0}{\tilde{P}_{\rm NL}}\frac{1}{T}\right), \tag{46a}$$

$$\frac{\partial^2 T}{\partial z^2}=\frac{4\beta_2}{k_0}\frac{E_0}{\tilde{P}_{\rm NL}}\frac{1}{R^2T^2}+\frac{4\beta_2^2}{T^3}+\frac{1}{\beta_2}\frac{\partial\beta_2}{\partial z}\frac{\partial T}{\partial z}, \tag{46b}$$

where $E_0=PT$ is proportional to the laser pulse energy and is independent of z, $P(z)=\pi R(z)^2I(z)/2$ is the laser power, $I(z)=cn_0B^2(z)/8\pi$ is the intensity, $\tilde{P}_{\rm NL}=P_{\rm NL}/4$ is the effective self-focusing power, and $P_{\rm NL}=\lambda_0^2/2\pi n_0n_2$ defines the usual self-focusing power. The method used to obtain Eqs. (46) involved equating powers of r and τ; a more rigorous derivation involving the source-dependent expansion method [53] would result in $\tilde{P}_{\rm NL}$ being equal to $P_{\rm NL}$. Hence, in numerical solutions of Eqs. (46) we set $\tilde{P}_{\rm NL}=P_{\rm NL}$. The first term on the right-hand side of Eq. (46a) describes vacuum diffraction while the second term describes nonlinear self-focusing, i.e., due to n_2. Nonlinear self-focusing dominates diffraction when $P>P_{\rm NL}$. The curvature parameter, chirp, phase, and energy evolve according to

$$\alpha(z)=-\frac{k_0R}{2}\frac{\partial R}{\partial z}, \tag{47a}$$

$$\beta(z)=\frac{T}{2\beta_2}\frac{\partial T}{\partial z}, \tag{47b}$$

$$\frac{\partial\theta}{\partial z}=-\frac{2}{k_0R^2}+\frac{\beta_2}{T^2}+\frac{1}{k_0R^2}\frac{P}{\tilde{P}_{\rm NL}}, \tag{47c}$$

$$\frac{\partial E_0}{\partial z}=0, \tag{47d}$$

respectively. Equation (47b) indicates that the pulse energy is conserved.

The general expression for the Fourier transform of the pulse amplitude is

$$\tilde{A}(r,z,\omega)=\int_{-\infty}^{\infty}d\tau A(r,z,\tau)\exp(i\omega\tau).$$

Using Eq. (45) we find that the Fourier pulse spectrum is given by

$$S(\omega)\sim\exp\left(-\frac{T^2(z)\omega^2}{4[1+\beta^2(z)]}\right). \tag{48}$$

The full Fourier spectral width at $1/e$ of the amplitude is

$$\Delta\omega(z)=\frac{4[1+\beta^2(z)]^{1/2}}{T(z)}, \tag{49}$$

where $\beta(z)$ is given by Eq. (47b). Using Eq. (47b) the instantaneous frequency spread, $\delta\omega(z,\tau)=2\beta(z)\tau/T^2(z)$, becomes

$$\delta\omega(z,\tau)=\frac{\tau}{\beta_2T(z)}\frac{\partial T(z)}{\partial z}. \tag{50}$$

Thus the frequency chirp vanishes along the entire pulse when the pulse length reaches a minimum.

For a spatially uniform neutral density and in the absence of nonlinear effects, i.e., $n_2=0$, the solution of Eq. (46b) is [34]

$$T(z)=T_0\left[\left(1+\beta_0\frac{z}{Z_T}\right)^2+\left(\frac{z}{Z_T}\right)^2\right]^{1/2}, \tag{51}$$

and the chirp parameter is

$$\beta(z)=\frac{T}{2\beta_2}\frac{\partial T}{\partial z}=\frac{1}{2\beta_2}\frac{T_0^2}{Z_T}\left[\beta_0+(1+\beta_0^2)\frac{z}{Z_T}\right], \tag{52}$$

where $T_0=T(0)$, $\beta_0=\beta(0)$, and $Z_T=T_0^2/2|\beta_2|$ is the group velocity dispersion length. Substituting Eqs. (51) and (52) into Eq. (49) yields $\Delta\omega=4(1+\beta_0^2)^{1/2}/T_0$, which indicates that for a linear atmosphere the Fourier spectral width is constant. In the absence of nonlinear effects, a minimum pulse length of $T_0/(1+\beta_0^2)^{1/2}$ is reached at $z/Z_T=-\beta_0/(1+\beta_0^2)$, provided the chirp parameter is initially negative, $\beta_0<0$.

In the limit that the pulse length does not change appreciably, it can be shown from Eq. (46a) that the variation of the spot size with propagation distance is given by

$$R(z)=R_0\left[1-2\alpha_0\frac{z}{Z_{R0}}+\left(\alpha_0^2-\frac{P}{\tilde{P}_{\rm NL}}+1\right)\left(\frac{z}{Z_{R0}}\right)^2\right]^{1/2}, \tag{53}$$

where $Z_{R0}=k_0R_0^2/2$. Equation (53) shows that when $P>\tilde{P}_{\rm NL}$, the spot size goes to zero in a distance

$$z/Z_{R0}=\frac{\alpha_0\pm\sqrt{(P/\tilde{P}_{\rm NL})-1}}{1-(P/\tilde{P}_{\rm NL})+\alpha_0^2}, \tag{54}$$

where the $\pm$ sign is chosen so that z is positive.

We compare the solutions of Eqs. (46) and (47) with the full numerical simulation. In the present example, propagation through a uniform air density is considered. The initial laser pulse at $z=0$ is described by Eq. (45) with $\lambda=0.775\ \mu$m, $R_0=1$ cm, $T_0=0.66$ psec, and $\beta_0=-20$ (a negative chirp with $|\delta\omega_{\rm full}/\omega_0|\approx0.05$), $\alpha_0=0$ (a collimated pulse), and initial peak intensity $I_0=10^9$ W/cm^2. In numerically solving Eqs. (46), the nonlinear index of air is taken to be $n_2=6\times10^{-19}$ cm^2/W, which is larger than the experimentally measured value of 3×10^{-19} cm^2/W [50]. This was

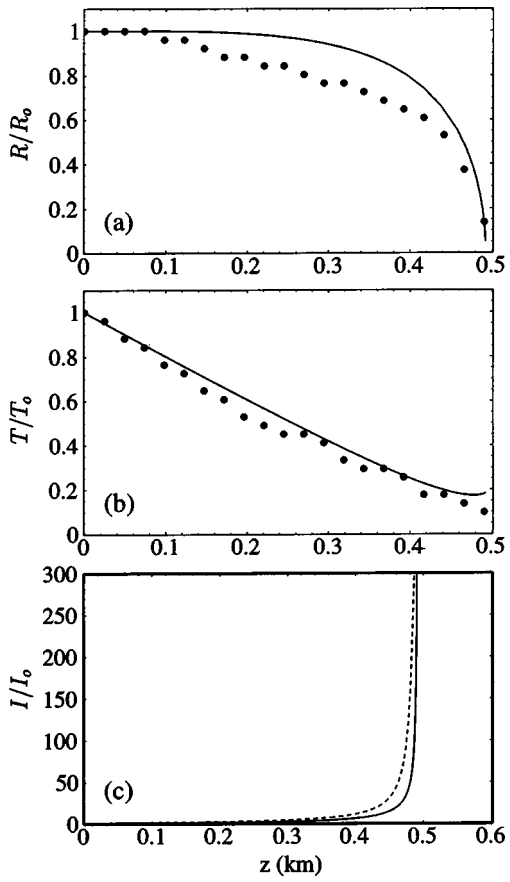

FIG. 10. Variation of (a) laser spot size, (b) pulse duration, and (c) peak intensity, from $z=0$ to 0.49 km, for a laser pulse with initial values $R_0=1$ cm, $T_0=0.66$ psec, $\beta_0=-20$, and $\alpha_0=0$. The initial peak intensity is $I_0=10^9$ W/cm^2 ($P_0/P_{\mathrm{NL}}=0.94$). Solid curves denote solutions of the envelope equations, i.e., Eqs. (46). Points in panels (a) and (b) and the dashed curve in panel (c) denote full scale simulation results.

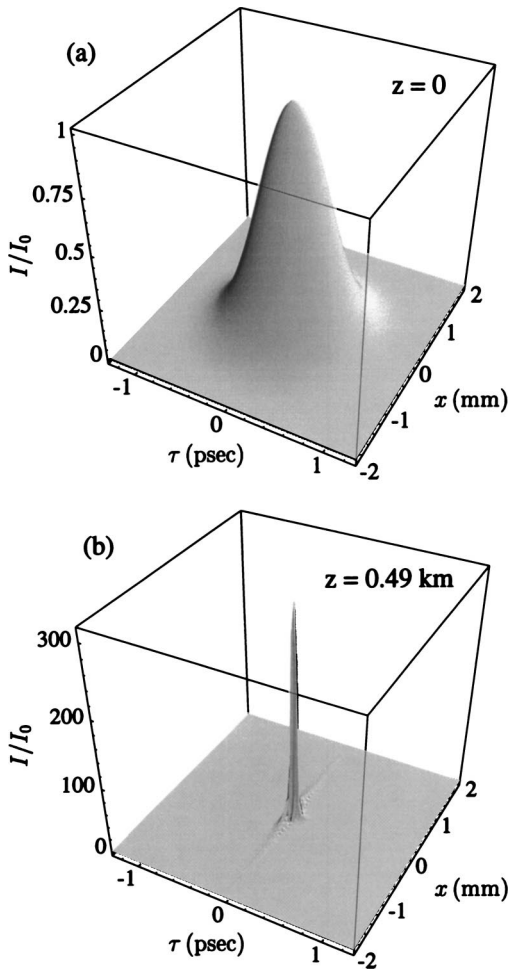

FIG. 11. Surface plots of the laser intensity at $z=0$ and $z=0.49$ km showing compression and focusing corresponding to the simulation of Fig. 9. Peak laser intensity increases by a factor of 300.

done in order to approximate the inclusion of Raman effects into the nonlinear refractive index. Raman effects can increase the nonlinear refractive index by an amount equal to the bound electron contribution, e.g., see Fig. 4. For these parameters, the focal distance for both longitudinal and transverse compression is expected to be $\sim$0.5 km, based on Eqs. (46). For the full simulation, which includes Raman effects, we take the nonlinear bound electron index to be $n_2=3\times10^{-19}$ cm^2/W, so that $P/P_{\mathrm{NL}}\sim0.5$ initially.

Figures 10(a) and 10(b) show the evolution of the laser spot and pulse duration as the focal point is approached. The pulse length decreases almost linearly with z by a factor of $\sim$10 from $z=0$ to $\sim$0.49 km. The spot size decreases at a slower rate from $z=0$ to $=$0.4 km and then falls rapidly over the last 0.1 km from focus. The corresponding evolution of the peak intensity is shown in Fig. 10(c). The intensity increases relatively slowly over most of the propagation path, gaining a factor of $\sim$10 over a distance of 0.4 km, and then increases rapidly by a factor of $>$30 in a distance of $\sim$0.1 km. The reduction in the spot size due to nonlinear self-focusing from $z=0.4$ to 0.49 km is mainly responsible for the enhanced intensity gain observed near the focal point. The results of the full simulation, denoted by the points in Figs. 10(a) and 10(b) and the dashed curve in Fig. 10(c), are in good agreement with the solution of Eqs. (47). Figure 11 shows surface plots of the distribution of laser intensity with τ and transverse coordinate x at $z=0$ and near focus at $z=0.49$ km obtained from the full simulation. The laser pulse focuses both longitudinally and transversely such that the peak laser intensity at $z=0.49$ km is $\sim3\times10^{11}$ W/cm^2, which is a factor of 300 larger than the initial intensity; note the change of scale between Figs. 11(a) and 11(b).

B. High-intensity propagation regime

When the laser pulse is sufficiently intense, $\sim10^{13}$ W/cm^2 for $\sim$100-fsec pulses, ionization processes, plasma defocusing, and Raman scattering effects become important. In this section, we simulate propagation of the laser pulse from the previous example through the region of plasma generation. The output of the previous simulation is extrapolated for $\sim$2 m using Eqs. (46) to numerically solve for the laser spot size, duration, and peak intensity close to the ionization region. The extrapolation was performed because of the computa-

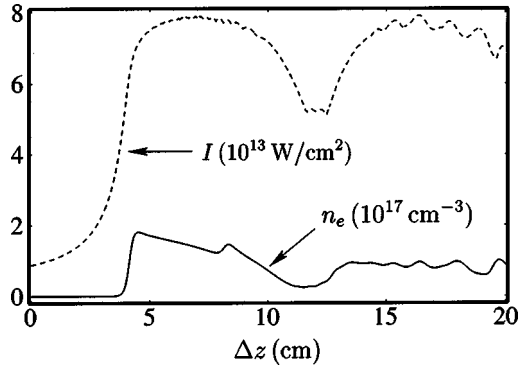

FIG. 12. Full scale simulation results showing the variation of peak laser intensity and peak plasma density with propagation distance in the vicinity of the focal region. The laser pulse at $\Delta z=0$ is characterized by $R=0.25$ mm, $T=120$ fsec, $\beta=7.2$, $\alpha=2$, and peak intensity $I=8.8\times10^{12}$ W/cm^2.

tional difficulty in using the full nonlinear simulation to accurately model the large variation of the spot size near the focal point. The extrapolated results are then used to initialize the Gaussian laser pulse in this high-intensity simulation which begins at $z_0=492$ m. The propagation distance Δz is measured relative to z_0, i.e., $\Delta z=z-z_0$. The pulse at $\Delta z=0$ is described by Eq. (45), with $R=0.25$ cm, $T=0.12$ psec, $\beta=7.2$, and $\alpha=2$. The initial peak intensity $I=8.8\times10^{12}$ W/cm^2 is below the intensity at which ionization effects become important. The initial ratio of the peak power to the nonlinear focusing power, $P/P_{\mathrm{NL}}=2.5$.

Figure 12 shows the evolution of the peak laser intensity and peak plasma density near the focal point. From $\Delta z=0$ to 5 cm, self-focusing causes the peak intensity to increase by a factor of ~8. As the laser intensity reaches the ionization threshold, a plasma channel is formed, which is highly localized near the laser pulse axis. The radius of the plasma channel is ~20 μm. Formation of a plasma channel counteracts the nonlinear focusing effect. From $\Delta z=5$ to 20 cm, the peak intensity is limited to $<7\times10^{13}$ W/cm^2 while the peak plasma density is on average $\sim7.5\times10^{16}$ cm^{-3}.

Figure 13 shows the evolution of the laser intensity profile from $\Delta z=6.3$ to 16.8 cm. The generation of a highly localized plasma channel at $\Delta z=4$ cm causes the trailing edge of the laser pulse to defocus and the pulse to shorten on axis, as shown in Fig. 13(a). Earlier parts of the pulse remain focused due to the absence of plasma. As the on-axis pulse length decreases, the plasma density also decreases, thereby allowing the trailing parts of the pulse (where $P>P_{\mathrm{NL}}$) to refocus. The refocusing of the trailing edge leads to the double-peaked intensity profile seen in Fig. 13(b). Subsequently, the intensity of the leading peak decreases due to diffraction until the intensity of the trailing peak becomes the global maximum [Fig. 13(c)]. At $\Delta z=16.8$ cm, the trailing peak is reconstituted in such a way that the laser intensity profile appears similar to that at $\Delta z=7.6$ cm. In earlier works [24] it was proposed that these recurrences underlie the experimentally observed long-distance propagation of intense pulses in air.

Since laser energy is lost to ionization whenever refocusing and plasma generation occur, the number of recurrences

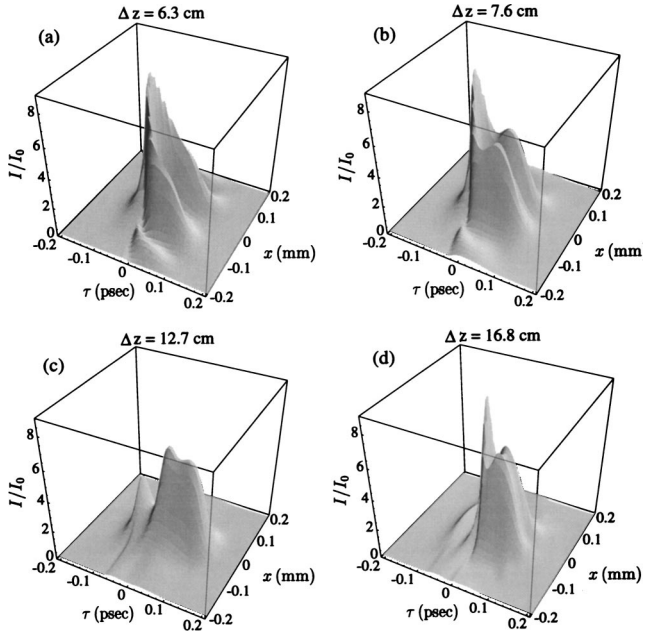

FIG. 13. Surface plots of laser intensity following the formation of plasma for the parameters described in the caption of Fig. 11.

will be limited. Refocusing will not be possible when the amount of energy lost to ionization is sufficient to cause the pulse power to become less than the nonlinear self-focusing power. Figure 14 shows the pulse energy as a function of propagation distance. The sudden decrease in energy at $\Delta z=5$ cm corresponds to the location at which a plasma density of $\sim10^{17}$ cm^{-3} is generated. From $\Delta z=5$ to 25 cm, $\sim7\%$ of the pulse energy is lost to ionization. Figure 15 shows the on-axis profile of the laser intensity and power (normalized to P_{NL}) at $\Delta z=16.5$ cm. The power profile at $\Delta z=16.5$ cm remains relatively unchanged from its initial Gaussian profile, indicating that there is little longitudinal energy transfer. Hence, the distortions in the laser intensity profile are caused mostly by transverse focusing. Note that a sufficient amount of power ($P\sim2P_{\mathrm{NL}}$) is present in the trailing edge of the pulse to allow for self-focusing. For this particular example, however, it is not possible to numerically simulate propagation beyond $\Delta z=25$ cm due to the large amount of spectral broadening that occurs, causing the theoretical model to become invalid; e.g., at $\Delta z=25$ cm, $|\delta\omega|\sim0.4\omega_0$.

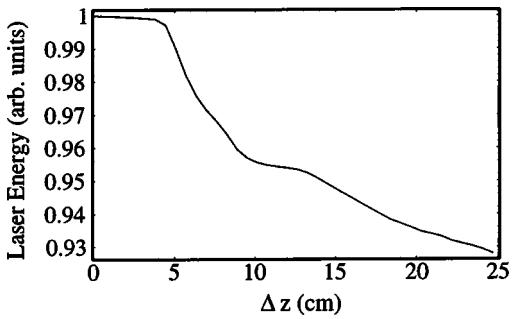

FIG. 14. Variation of laser energy with propagation distance in the region of plasma formation for the simulation of Fig. 11.

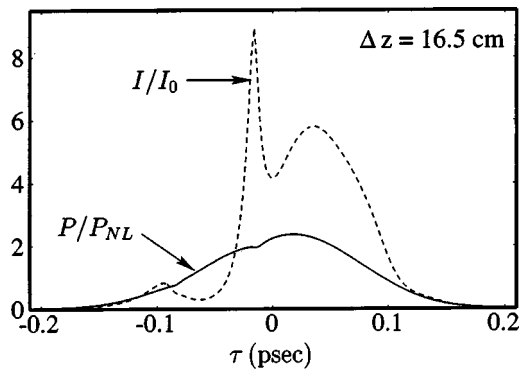

FIG. 15. Normalized, on-axis profile of laser intensity (I/I_0) and power (P/P_{NL}) at propagation distance $\Delta z = 16.5$ cm for the simulation of Fig. 11.

Figure 16 shows that the on-axis Fourier spectrum of the laser pulse broadens with propagation distance. The asymmetry of the spectrum, i.e., the more prominent redshift, is associated with the gradient of the laser intensity becoming larger at the front of the pulse than at the back [34]. At $\Delta z = 17.7$ cm, the blue-shifted part of the spectrum is sufficiently broad that it spans the visible spectrum indicating that white light is generated near the focal point. Modulations in the spectrum, which are prominent at $\Delta z = 15.2$ cm, are caused by a self-interference effect that can be understood as follows. Initially, every axial position within the chirped laser pulse has a different frequency, as shown in Fig. 17(a). As the pulse propagates, Fig. 17(b) shows that distortions in the laser envelope cause different axial positions of the pulse to have the same frequency. These positions represent waves with the same frequency but with different phases that can interfere constructively or destructively depending on the relative phase difference. This interference results in multipeak structures in the spectrum [57].

C. Vertical propagation, compression, and focusing

We use Eqs. (46) to examine propagation in a spatially varying atmosphere. The spatial variation of air density is given by $n_a(z) = n_a(0)\exp(-z/L_a)$, where $n_a(0) = 2.7 \times 10^{19}\ \mathrm{cm}^{-3}$ is the neutral density at sea level, and $L_a = 8$ km is the characteristic scale for the upward variation of the air density. The initial laser pulse is characterized by

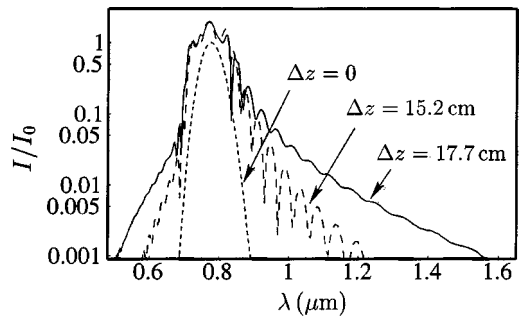

FIG. 16. Fourier spectrum of laser intensity as a function of wavelength at propagation distances $\Delta z = 0$, 15.2, and 17.7 cm for the simulation of Fig. 11.

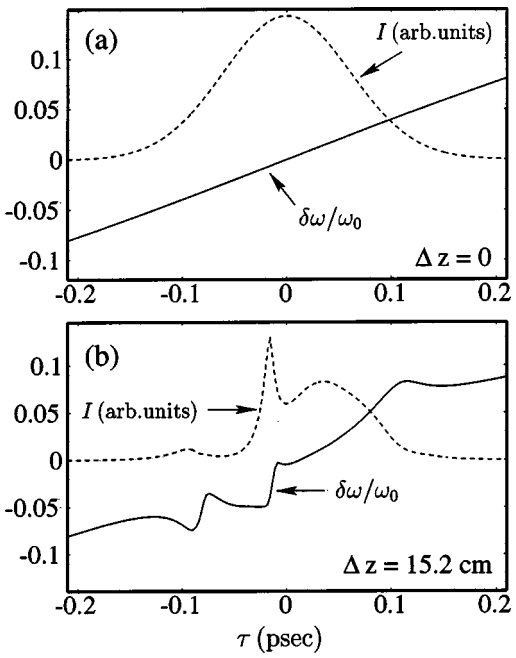

FIG. 17. Intensity profile (dashed curves) and normalized instantaneous frequency spread ($\delta\omega/\omega_0$) of the laser pulse at (a) $\Delta z = 0$ and (b) $\Delta z = 15.2$ cm corresponding to the spectra of Fig. 15.

$R_0 = 28$ cm, $T_0 = 5$ psec, $I_0 = 3.2 \times 10^6$ W/cm^2, $\lambda = 1.06$ μm, $\beta_o = -46$ (a negative chirp with $|\delta\omega_{\mathrm{full}}|/\omega_0 \approx 0.02$), and $\alpha_o = 10$ (a focusing beam). The dashed curve in Fig. 18(a) shows the altitude variation of the air density. The solid curve shows the evolution of the peak laser intensity (normalized to its value at $z = 0$) with altitude. For these parameters the focal length, i.e., the distance at which the pulse duration and spot size are simultaneously minimized, is ~21 km. The intensity increases by a factor of 2×10^4 at focus. Most of the intensity gain occurs within 5 km of the focal region where the density of air is relatively low.

Figure 18(b) shows the variation of laser spot size and pulse duration with z. From $z = 0$ to ~20 km, the spot size decreases linearly with z, indicating that the transverse focusing is mostly linear, i.e., due to the wave front curvature of the pulse. Nonlinear self-focusing becomes dominant over the final 2 km of propagation and causes the spot size to decrease more rapidly. In the absence of ionization and other higher-order nonlinearities, the spot size collapses to zero at $z \sim 22$ km. The pulse duration decreases continually due to group velocity dispersion, and is reduced by a factor of ~1/20 in the focal region.

VI. SUMMARY

In this paper we have investigated a number of key physical processes associated with short, intense laser pulses propagating in the atmosphere. Some of the potential applications stem from the possibility of creating an atmospheric ''lamp'' at a remote location with spectral characteristics that are similar to a white light source [4,8,9]. The applications range from remote sensing and ultraviolet fluorescence spec-

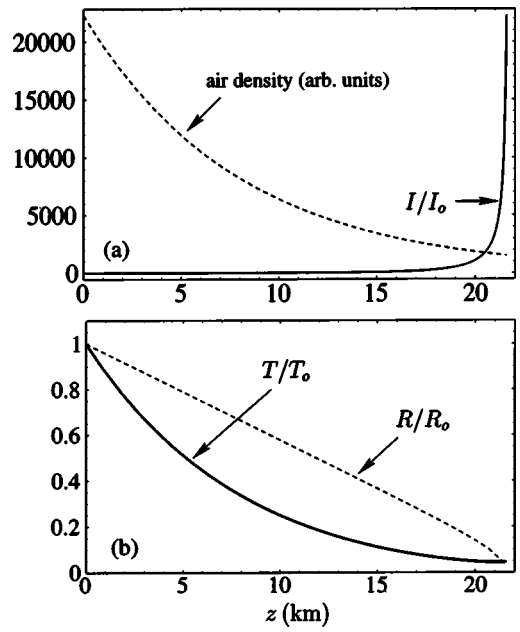

FIG. 18. (a) Dependence of air density (dashed curve) and peak laser intensity (solid curve) on z (altitude). (b) Normalized laser spot size (dashed curve) and pulse duration (solid curve) as a function of altitude. Evolution of the laser spot size, pulse duration, and peak intensity for the given density profile are calculated using Eqs. (46). Initial conditions are given by $R_0=28$ cm, $T_0=5$ psec, $I_0=3.2\times10^6$ W/cm^2, $\lambda=1.06$ μm, $\beta_0=-46$ (a negative chirp with $|\delta\omega_{\rm full}|/\omega_0\approx0.02$), and $\alpha_0=10$.

troscopy to electromagnetic countermeasures, hyperspectral imaging, differential absorption spectroscopy, and induced atmospheric electrical discharges (artificial lightning) [10–18,58].

Nonlinear equations have been derived which include dispersion, nonlinear self-focusing, stimulated molecular rotational Raman scattering, multiphoton and tunneling ionization, pulse energy depletion due to ionization, atmospheric nonuniformity, relativistic focusing, and plasma wakefield generation. The nonlinear equations have been used to analyze a number of phenomena, such as the compression and focusing of chirped laser pulses, laser filamentation, and white light generation.

The variation of the nonlinear refractive index and instantaneous frequency shift along an intense laser pulse in air has been calculated. The analytical results have been obtained by assuming a self-similar form for the laser envelope and deriving coupled envelope equations for the amplitude, phase, curvature, and spot size. As an example, for a ~500-fsec laser pulse, the frequency shifts associated with bound electrons, ionization, and Raman scattering are found to be comparable. The combined effects of bound electron nonlinearities, ionization, and Raman scattering produce a redshift at the front of the pulse and a larger blue shift at the back.

Using the SDE a coupled set of equations for the spot size, laser power, and electron density is derived. A necessary condition for an approximate equilibrium of a single optical filament has been derived, assuming that the ionization rate is low. The equilibrium involves a balancing between nonlinear self-focusing, diffraction, and plasma defocusing, and is shown to require a specific distribution of power along the filament. For the approximate equilibrium, the laser power at the head of the pulse equals the nonlinear focusing power, and increases towards the back of the pulse. The increase in power is necessary to counteract the effect of plasma defocusing. When the laser intensity is sufficiently high to cause considerable energy depletion due to ionization, an equilibrium solution no longer exists and self-guided propagation is not possible. Numerical solutions of the SDE equations show that a ~100-fsec laser pulse can propagate in a self-guided mode for ~10 Rayleigh lengths, after which plasma defocusing erodes the front and back of the pulse. This defocusing leads to the formation of a very short ~5-fsec pulse that can propagate for ~100 Rayleigh lengths.

A method for generating a remote spark in the atmosphere has been proposed and investigated. This method utilizes the dispersive and nonlinear properties of air to cause a low-intensity chirped laser pulse to compress both longitudinally and transversely. For optimally chosen parameters, the transverse and longitudinal focal lengths can be made to spatially coincide resulting in a rapid intensity increase, ionization, and white light generation in a localized region far from the source.

Solutions of the envelope equations are found to agree well with full 3D simulations in the low-intensity propagation regime far from the focal region. Near the focal spot where the intensity is large enough to ionize air, plasma filaments can be generated in a region ~1 m in extent and significant white light generation occurs.

ACKNOWLEDGMENTS

The authors acknowledge useful discussions with C. Kapetanakos, R. F. Hubbard, R. Fernsler, S. Slinker, A. Ting, D. Gordon, and A. Zigler. This work was supported by the Office of Naval Research and the Joint Technology Office in support of the Navy Directed Energy Weapons Program Office.

APPENDIX: DERIVATION OF NONLINEAR SOURCE TERMS

In this Appendix the nonlinear source amplitude given by Eq. (6) is derived. It is convenient to write the nonlinear source term as

$$\mathbf{S}_{\rm NL}(\mathbf{r},t)=\mathbf{S}_{\rm bound}+\mathbf{S}_{\rm Raman}+\mathbf{S}_{\rm plasma}+\mathbf{S}_{\rm wake}+\mathbf{S}_{\rm rel}+\mathbf{S}_{\rm ion}$$
$$=S_{\rm NL}(\mathbf{r},t)e^{i\psi(z,t)}\mathbf{e}_x/2+\text{c.c.}, \tag{A1}$$

where the various contributions, $\mathbf{S}_{\rm bound}$, $\mathbf{S}_{\rm Raman}$, $\mathbf{S}_{\rm plasma}$, $\mathbf{S}_{\rm wake}$, $\mathbf{S}_{\rm rel}$, and $\mathbf{S}_{\rm ion}$, represent, respectively, contributions from the third-order nonlinearity associated with bound electrons, stimulated Raman scattering, plasma generation, wakefields, relativistic motion of free electrons, and laser energy depletion due to ionization. The various source terms are derived in the following sections.

1. Nonlinear polarization of bound electrons

In general, the nonlinear source term due to bound electrons, Kerr effect, is

$$\mathbf{S}_{\text{bound}}(r,z,t) = 4\pi c^{-2}\partial^2 \mathbf{P}_{\text{bound}}(\mathbf{r},t)/\partial t^2 = \mathbf{S}_{\text{bound}}(\mathbf{r},t)e^{i\psi(z,t)}\hat{\mathbf{e}}_x/2 + \text{c.c.}, \quad \text{(A2)}$$

where the phase is $\psi(z,t) = k_0 z - \omega_0 t$. The nonlinear polarization field is given by [34–36]

$$\mathbf{P}_{\text{bound}}(\mathbf{r},t) = \chi_{\text{NL}}\langle \mathbf{E}\cdot\mathbf{E}\rangle_t \mathbf{E}(\mathbf{r},t), \quad \text{(A3)}$$

where χ_{NL} is the scalar third-order susceptibility of the neutral gas and the brackets $\langle\rangle_t$ denote a time average. In this approximation the third harmonic component of the nonlinear polarization field is neglected and the nonlinear response is assumed to be instantaneous. The refractive index is the sum of the linear and nonlinear contributions, and in the absence of relativistic effects is expressible as

$$n(r,\omega) = n_0(r,\omega) + n_2 I, \quad \text{(A4)}$$

where I is the time-averaged intensity and n_2 is the nonlinear refractive index associated with bound electrons. Equation (A3) can be expressed in terms of n_2, i.e.,

$$\mathbf{P}_{\text{bound}}(\mathbf{r},t) = \frac{1}{4\pi}[2n_0 n_2 I(\mathbf{r},t)]\mathbf{E}(\mathbf{r},t) = \left(\frac{n_0}{4\pi}\right)^2 c n_2 |A(\mathbf{r},t)|^2 \mathbf{E}(\mathbf{r},t), \quad \text{(A5)}$$

where n_0 is the linear index, $n_2 = (8\pi^2/n_0^2 c)\chi_{\text{NL}}$, $I(\mathbf{r},t) = (c/4\pi)n_0\langle \mathbf{E}\cdot\mathbf{E}\rangle_t = c n_0 |A|^2/8\pi$ is the intensity, and $|n_2 \mathbf{I}| \ll n_0 - 1$ has been assumed. Substituting Eq. (A5) into (A2) and using the envelope representation for $\mathbf{E}(\mathbf{r},t)$, i.e., Eq. (2a), the amplitude of the nonlinear source term is

$$S_{\text{bound}}(r,z,t) = \frac{\omega_0^2 n_0^2 n_2}{4\pi c}|A(\mathbf{r},t)|^2 A(\mathbf{r},t). \quad \text{(A6)}$$

2. Stimulated nonresonant Raman scattering

Stimulated Raman scattering of laser pulses propagating through air has been studied extensively [28,59–69]. For altitudes below 100 km, the dominant Raman process for long pulses (~nsec) is due to scattering from N_2 molecules involving the $S(8)$ rotational transition from the $J=8$ to $J=6$ rotational states, while the molecule remains in the vibrational ground state [61]. For a linearly polarized laser with wavelength 1.05 μm, experiments using long (~nsec) pulses indicate that the Raman gain coefficient is ~2.5 cm/TW [28]. The observed Raman shift for the $S(8)$ rotational transition is 75 cm^{-1} ($\Delta\omega \sim 14\times 10^{12}$ sec^{-1}) while the characteristic relaxation time for excited states is typically 0.1 nsec at sea level. A number of experimental studies have employed shorter (~100 fsec) laser pulses to investigate Raman scattering. In particular, the gain coefficient and damping rate have been measured and found to be different from those appropriate for longer pulses [50].

The theoretical model used here to incorporate the effects of stimulated rotational Raman scattering into the general nonlinear propagation equation is based on the standard density matrix formalism [70] with an envelope representation for the laser electric field, i.e., $\mathbf{E}(\mathbf{r},t) = (1/2)A(\mathbf{r},t)e^{i\psi(z,t)}\hat{\mathbf{e}}_\perp + \text{c.c.}$, where $A(\mathbf{r},t)$ is the complex amplitude, $\hat{\mathbf{e}}_\perp$ denotes a unit vector in the polarization direction, and c.c. denotes the complex conjugate. The envelope representation allows for the generation of a multiwave Raman spectrum, i.e., harmonics of the Stokes and anti-Stokes sidebands, as well as broadening of the individual lines. The model also describes the Raman response in the transient regime, and accounts for the natural damping or relaxation of excited states and saturation due to the population depletion of the ground state.

Stimulated Raman scattering is associated with a nonlinear polarization field $\mathbf{P}_{\text{Raman}}(\mathbf{r},t) = P_{\text{Raman}}(\mathbf{r},t)e^{i\psi(z,t)}\hat{\mathbf{e}}_x/2 + \text{c.c.}$, which gives rise to a source term in the propagation equation for the laser envelope. The nonlinear source term is expressed in terms of the nonlinear polarization as

$$\mathbf{S}_{\text{Raman}}(r,z,t) = 4\pi c^{-2}\partial^2 \mathbf{P}_{\text{Raman}}(\mathbf{r},t)/\partial t^2 = S_{\text{Raman}}(\mathbf{r},t)e^{i\psi(z,t)}\hat{\mathbf{e}}_x/2 + \text{c.c.} \quad \text{(A7)}$$

It is assumed that the rotational states of a molecule can be represented as a three-level system with energy levels W_1 and W_2, and an excited state (e.g., an electronic or translational state) with energy $W_3 \gg W_2 - W_1$. Since the eigenstates are assumed to possess definite parity, direct transitions between states 1 and 2 are forbidden. It is also assumed that the Raman processes is nonresonant, so that state 3 is not populated. Under these assumptions, it can be shown using the standard density matrix formalism [70] that the nonlinear polarization can be represented as

$$P_{\text{Raman}} = \chi_L Q(t) A(\mathbf{r},t), \quad \text{(A8)}$$

where $Q(t)$ is the unitless oscillator function which is determined by the system of equations

$$\frac{\partial^2 Q}{\partial t^2} + (\omega_R^2 + \Gamma_2^2)Q + 2\Gamma_2 \frac{\partial Q}{\partial t} = -\omega_R \frac{\Omega_R^2}{\Omega} W(t)\frac{|A(\mathbf{r},t)|^2}{A_0^2}, \quad \text{(A9)}$$

$$\frac{\partial W}{\partial t} = \frac{\Omega_R^2}{\omega_R \Omega}\frac{|A(\mathbf{r},t)|^2}{A_0^2}\left(\frac{\partial Q}{\partial t} + \Gamma_2 Q\right) - \Gamma_1(W - W_0), \quad \text{(A10)}$$

where $\Omega_R = \mu A_0/\hbar$ is the Rabi frequency associated with the peak laser amplitude A_0 and μ is the dipole transition moment matrix element associated with transitions to state 3. The quantities Γ_1 and Γ_2 are phenomenological damping rates that have been included heuristically. The quantity W is the difference between the normalized population densities of states 2 and 1, and $W_0 = W(t \to -\infty)$. For a medium in which all molecules are initially in the ground state, $W_0 = -1$.

Assuming a slowly varying amplitude for the polarization, i.e., $|\partial^2 P_{\rm Raman}/\partial t^2| \ll \omega_0^2 |P_{\rm Raman}|$, the source term for stimulated Raman scattering is given by

$$S_{\rm Raman} = -4\pi \frac{\omega_0^2}{c^2} \chi_L Q(\mathbf{r},t) A(\mathbf{r},t). \tag{A11}$$

The solution of Eq. (A9) can be rewritten in the form

$$Q(\mathbf{r},t) = -\frac{n_R n_0}{2\pi\chi_L} \int_{-\infty}^{t} dt' W(t') R(t-t') I(\mathbf{r},t'), \tag{A12}$$

where

$$R(t) = \left(\frac{\omega_R^2 + \Gamma_2^2}{\omega_R} \right) e^{-\Gamma_2 t} \sin(\omega_R t), \tag{A13a}$$

is the Green's function for the Raman process,

$$n_R = \frac{16\pi^2 \chi_L}{c n_0^2 \Omega} \frac{\mu^2}{\hbar^2} \frac{\omega_R}{\omega_R^2 + \Gamma_2^2}, \tag{A13b}$$

is the Raman contribution to the nonlinear index for long duration pulses ($\tau > \Gamma_2, \omega_R$), and $R(t)$ is normalized such that $\int_0^\infty dt R(t) = 1$. If only the Raman source term is retained on the right-hand side of Eq. (15), it can be shown through a stability analysis [35,36] that an initial Stokes perturbation $\delta A(z=0)$ on a cw pump laser beam can grow exponentially, i.e., $\Delta A(z) = \delta A(0) \exp(g I_p z)$, with a maximum gain coefficient

$$g = \frac{8\pi^2}{c} \frac{\chi_L}{n_0^2} \frac{\mu^2}{\hbar^2} \frac{\omega_0}{c} \frac{1}{\Omega \Gamma_2}, \tag{A14}$$

where I_p is the pump intensity. Stokes–anti-Stokes coupling will reduce the gain coefficient.

The nonlinear polarization field in Eq. (A8) has a contribution that is third order in the field amplitude, and thus can contribute to the total nonlinear refractive index. Including the bound electron and molecular Raman response, the total nonlinear refractive index is

$$n_{\rm NL}(\mathbf{r},t) = n_2 I(\mathbf{r},t) - n_R \int_{-\infty}^{t} dt' W(t') R(t-t') I(\mathbf{r},t'). \tag{A15}$$

For a constant amplitude laser pulse with duration τ_L, the field amplitude can be written as $A = A_0[\Theta(\tau) - \Theta(\tau - \tau_L)]$, where $\tau = t - z/c$. We assume that there is negligible population inversion, $W(\tau) \approx -1$. With these approximations, Eqs. (A13) and (A14) indicate that the total nonlinear index within the pulse, i.e., $0 < \tau < \tau_L$, is

$$n_{\rm NL}(\tau) = n_2 + n_R\{1 - e^{-\Gamma_2 \tau}[\cos(\omega_R \tau) + (\Gamma_2/\omega_R)\sin(\omega_R \tau)]\}, \tag{A16}$$

where n_R can be written in terms of the gain,

$$n_R = 2 \frac{\omega_R}{\omega_0} \frac{\Gamma_2}{\omega_R^2 + \Gamma_2^2} c g. \tag{A17}$$

In the long-pulse limit ($\tau \gg 1/\Gamma_2$), n_R represents the effective nonlinear index due to Raman effects, and the total nonlinear refractive index is $n_{\rm NL} = n_2 + n_R$. For shorter pulses, compared with the characteristic Raman times ($\tau \ll 1/\omega_R$, $\tau \ll 1/\Gamma_2$), the nonlinear refractive index is due purely to the bound electron response, i.e., $n_{\rm NL} = n_2$.

Experiments suggest that the Raman response is a sensitive function of the pulse duration. For a long (~nsec) laser with wavelength 1 μm ($\omega_0 = 1.9 \times 10^{15}$ sec^{-1}), the rotational Raman response is dominated by the $S(8)$ rotational transition from $J=8$ to $J=6$, which is characterized by $\omega_R \sim 1.4 \times 10^{13}$, $\Gamma_2 \sim 10^{10}$ sec^{-1}, and $g \sim 2.5$ cm/TW for air at STP [28,62]. For these parameters, the nonlinear refractive index due to rotational Raman processes is $n_R = 5.6 \times 10^{-20}$ cm^2/W. Assuming that bound electron and Raman effects are the dominant contributions to the nonlinear refractive index, the empirically determined value of $n_{\rm NL} \approx n_2 + n_R$ in the long-pulse regime is $\sim 5.6 \times 10^{-19}$ cm^2/W, giving $n_R/n_{\rm NL} \approx 0.1$. More recent experiments, which propagate much shorter ~100-fsec laser pulses with wavelength $\lambda = 0.8$ μm through air, suggest that the effective parameters for the short-pulse regime are $\omega_R \approx 1.6 \times 10^{13}$ sec^{-1}, $n_R \approx n_2 \approx 3 \times 10^{-19}$ cm^2/W, and $\Gamma_2 \approx 1.3 \times 10^{13}$ sec^{-1} [50], giving an effective gain coefficient of $g \approx 0.025$ cm/TW.

3. Plasma, wakefield, and relativistic source terms

The source term in the wave equation due to the motion of free electrons is given by $\mathbf{S}_{\rm free} = (4\pi/c^2)\partial \mathbf{J}/\partial t$, where the plasma current density $\mathbf{J}$ satisfies the equation

$$\frac{\partial \mathbf{J}}{\partial t} + \nu_e \mathbf{J} = \frac{\omega_p^2}{4\pi} \left(1 + \frac{\delta n_e}{n_e} \right) \mathbf{E}(\mathbf{r},t). \tag{A18}$$

In Eq. (A18), $\omega_p(\mathbf{r},t) = (4\pi q^2 n_e(\mathbf{r},t)/m)^{1/2}$ is the plasma frequency, $n_e(\mathbf{r},t)$ is the electron density, $\delta n_e(\mathbf{r},t)$ is the plasma density perturbation due to wakefields, and ν_e is the collision frequency of electrons. For air $\nu_e \approx 3 \times 10^{12}$ sec^{-1} [19,24]. Equation (A18) is valid even if the plasma density is increasing because of ionization. It can be shown that the electric field associated with $\delta n_e(\mathbf{r},t)$ satisfies the equation [71]

$$\left[\frac{\partial^2}{\partial t^2} + c^2 \nabla \times \nabla \times + \omega_p^2(\mathbf{r},t) \right] \mathbf{E}_w = \frac{q}{4m} \frac{\omega_p^2(\mathbf{r},t)}{\omega_0^2} \nabla |A|^2. \tag{A19}$$

The wakefield density perturbation is then obtained from $\delta n_e = \nabla \cdot \mathbf{E}_W / 4\pi q$. Writing the laser electric field and plasma source terms as $\mathbf{E}(\mathbf{r},t) = A(\mathbf{r},t) e^{i\psi(z,t)} \hat{\mathbf{e}}_x/2 + \text{c.c.}$ and $\mathbf{S}_{\rm free}(r,z,t) = S_{\rm free}(\mathbf{r},t) e^{i\psi(z,t)} \hat{\mathbf{e}}_x/2 + \text{c.c.}$, respectively, Eq. (A18) yields

$$S_{\rm free} = \frac{\omega_p^2(\mathbf{r},t)}{c^2} \left(1 + \frac{\delta n_e}{n_e} - \frac{\delta m}{m} \right) \left(1 - i \frac{\nu_e}{\omega_0} \right) A(\mathbf{r},t). \tag{A20}$$

In writing Eq. (A20), the plasma current density **J** was obtained to order $\nu_e/\omega_0 \ll 1$. The plasma frequency in Eq. (A20) contains contributions from ionization and relativistic electron motion. In order to write out each contribution explicitly, the electron mass is written as $m+\delta m$, where m is the electron rest mass and δm is the modification due to relativistic motion of the electron in the laser field. To second order in the field amplitude, the fractional change in the electron's mass is

$$\delta m/m = \frac{1}{4}\left(\frac{q}{mc\omega_0}\right)^2 |A(\mathbf{r},t)|^2. \tag{A21}$$

In writing Eq. (A21) it has been assumed that $|qA/mc\omega_0| \ll 1$, i.e., the weakly relativistic limit. The magnitude of $qA/mc\omega_0$ is often referred to as the laser strength parameter. For a linearly polarized laser beam, $|qA/mc\omega_0| = 8.6 \times 10^{-10}(\lambda[\mu\mathrm{m}])(I^{1/2}[\mathrm{W/cm^2}])$, where λ is the wavelength in microns and I is the intensity in W/cm^2.

Using Eq. (A21), Eq. (A20) can be written explicitly as $S_{\mathrm{free}} = S_{\mathrm{plasma}} + S_{\mathrm{rel}} + S_{\mathrm{wake}}$, where

$$S_{\mathrm{plasma}} = \frac{\omega_p^2(\mathbf{r},t)}{c^2}\left(1-\frac{\nu_e}{\omega_0}\right)A(\mathbf{r},t), \tag{A22a}$$

$$S_{\mathrm{rel}} = -\frac{\omega_p^2(\mathbf{r},t)}{4c^2}\left(\frac{q|A(\mathbf{r},t)|}{mc\omega_0}\right)^2 A(\mathbf{r},t), \tag{A22b}$$

$$S_{\mathrm{wake}} = \frac{\omega_p^2(\mathbf{r},t)}{c^2}\,\frac{\delta n_e}{n_e}A(\mathbf{r},t), \tag{A22c}$$

where it has been assumed that $\delta m/m \ll 1$, $\nu_e/\omega_0 \ll 1$, and $|\delta n_e|/n_e \ll 1$.

4. Laser energy depletion due to ionization

To derive the source term describing the depletion of the laser energy due to ionization, we note that the rate of change of the total field energy (electric and magnetic) due to only ionization is

$$\frac{\partial W_f}{\partial z} = U_{\mathrm{ion}} \int n_e(x,y,z,\tau)\, d\sigma, \tag{A23}$$

where W_f is the total field energy, U_{ion} is the effective ionization energy, and $d\sigma$ is the differential cross sectional area. The total field energy can be written as

$$W_f = -\int d\sigma \int d(c\tau)\langle \mathbf{E}\cdot\mathbf{E}\rangle_t/4\pi, \tag{A24}$$

where $\langle\ \rangle_t$ denotes a time average, $\langle \mathbf{E}\cdot\mathbf{E}\rangle_t = |A|^2/2$, and $-c\,d\tau$ is the differential in the z direction. Substituting Eq. (A24) into Eq. (A23), we find that

$$\frac{\partial |A|^2}{\partial z} = -8\pi U_{\mathrm{ion}}\frac{\partial n_e}{\partial c\tau}. \tag{A25}$$

Equation (A25) accounts for field energy lost due to ionization, and indicates that an additional source term given by

$$S_{\mathrm{ion}} = -8\pi i k_0 \frac{U_{\mathrm{ion}}}{|A|^2}\,\frac{\partial n_e}{\partial c\tau}A \tag{A26}$$

should be present to properly account for energy depletion.

[1] A. Braun, G. Korn, X. Liu, D. Du, J. Squier, and G. Mourou, Opt. Lett. **20**, 73 (1995).

[2] E. T. Nibbering, P. F. Curley, G. Grillon, B. S. Prade, M. A. Franco, F. Salin, and A. Mysyrowicz, Opt. Lett. **21**, 1 (1996).

[3] O. G. Kosareva, V. P. Kandidov, A. Brodeur, C. Y. Chien, and S. L. Chin, Opt. Lett. **22**, 1332 (1997).

[4] L. Woste, C. Wedekind, H. Wille, P. Rairoux, B. Stein, S. Nikolov, Ch. Werner, St. Niedermeier, F. Ronneberger, H. Schillinger, and R. Sauerbrey, Laser Optoelektron. **29**, 51 (1997).

[5] B. La Fontaine, F. Vidal, Z. Jiang, C. Y. Chien, D. Comtois, A. Desparois, T. W. Johnston, J.-C. Kieffer, H. Pepin, and H. P. Mercure, Phys. Plasmas **6**, 1615 (1999).

[6] S. Tzortzakis, L. Berge, A. Couairon, M. Franco, B. Prade, and A. Mysyrowicz, Phys. Rev. Lett. **86**, 5470 (2001).

[7] C. Y. Chien, B. La Fontaine, A. Desparois, Z. Jiang, T. W. Johnston, J.-C. Kieffer, H. Pepin, F. Vidal, and H. P. Mercure, Opt. Lett. **25**, 578 (2000).

[8] J. Kasparian, R. Sauerbrey, D. Mondelain, S. Niedermeier, J. Yu, J.-P. Wolf, Y.-B. Andre, M. Franco, B. Prade, S. Tzortzakis, A. Mysyrowicz, M. Rodriguez, H. Wille, and L. Woste, Opt. Lett. **25**, 1397 (2000).

[9] J. Yu, D. Mondelain, G. Ange, R. Volk, S. Niedermeier, J. P. Wolf, J. Kasparian, and R. Sauerbrey, Opt. Lett. **26**, 533 (2001).

[10] X. M. Zhao, J.-C. Diels, C. Y. Wang, and J. M. Elizondo, IEEE J. Quantum Electron. **31**, 599 (1995).

[11] H. Schillinger and R. Sauerbrey, Appl. Phys. B: Lasers Opt. **68**, 753 (1999).

[12] S. Tzortzakis, M. A. Franco, Y.-B. Andre, A. Chiron, B. Lamouroux, B. S. Prade, and A. Mysyrowicz, Phys. Rev. E **60**, R3505 (1999).

[13] D. Comtois, C. Y. Chien, A. Desparois, F. Genin, G. Jarry, T. W. Johnston, J.-C. Kieffer, B. La Fontaine, F. Martin, R. Mawassi, H. Pepin, F. A. M. Rizk, F. Vidal, P. Couture, H. P. Mercure, C. Potvin, A. Bondiou-Clergerie, and I. Gallimberti, Appl. Phys. Lett. **76**, 819 (2000).

[14] H. D. Ladouceur, A. P. Baronavski, D. Lohrmann, P. W. Grounds, and P. G. Girardi, Opt. Commun. **189**, 107 (2001).

[15] A. Proulx, A. Talebpour, S. Petit, and S. L. Chin, Opt. Commun. **174**, 305 (2000).

[16] C.-C. Cheng, E. W. Wright, and J. V. Moloney, Phys. Rev. Lett. **87**, 213001 (2001).

[17] P. Rairoux, H. Schillinger, S. Niedermeier, M. Rodriguez, F. Ronneberger, R. Sauerbrey, B. Stein, D. Waite, C. Wedekind,

H. Wille, L. Woste, and C. Ziener, Appl. Phys. B: Lasers Opt. **B71**, 573 (2000); P. A. Bernhardt, J. Opt. Soc. Am. A **12**, 1884 (1995).

[18] G. Faye, J. Kasparian, and R. Sauerbrey, Appl. Phys. B: Lasers Opt. **B73**, 157 (2001).

[19] M. D. Feit and J. A. Fleck, Appl. Phys. Lett. **24**, 169 (1974).

[20] P. Sprangle, E. Esarey, and J. Krall, Phys. Rev. E **54**, 4211 (1996).

[21] A. Brodeur, C. Y. Chien, F. A. Ilkov, S. L. Chin, O. G. Kosareva, and V. P. Kandidov, Opt. Lett. **22**, 304 (1997).

[22] H. R. Lange, G. Grillon, J.-F. Ripoche, M. A. Franco, B. Lamouroux, B. S. Prade, A. Mysyrowicz, E. T. J. Nibbering, and A. Chiron, Opt. Lett. **23**, 120 (1998).

[23] N. Akozbek, M. Scalora, C. M. Bowden, and S. L. Chin, Opt. Commun. **191**, 353 (2001); N. Akozbek, C. M. Bowden, A. Talebpour, and S. L. Chin, Phys. Rev. E **61**, 4540 (2000).

[24] M. Mleinek, E. M. Wright, and J. V. Moloney, Opt. Lett. **23**, 382 (1998); M. Mlejnek, E. M. Wright and J. V. Moloney, Phys. Rev. E **58**, 4903 (1998); M. Mlejnek, E. M. Wright, and J. V. Moloney, Opt. Express **4**, 223 (1999); M. Mlejnek, M. Kolesik, J. V. Moloney, and E. M. Wright, Phys. Rev. Lett. **83**, 2938 (1999).

[25] J. Kasparian, R. Sauerbrey, and S. L. Chin, Appl. Phys. B: Lasers Opt. **B71**, 877 (2000).

[26] A. Couairon and L. Berge, Phys. Plasmas **7**, 193 (2000).

[27] E. Esarey, G. Joyce, and P. Sprangle, Phys. Rev. A **44**, 3908 (1991); P. Sprangle and E. Esarey, Phys. Fluids B **4**, 2241 (1992).

[28] M. Henesian, C. D. Swift, and J. R. Murray, Opt. Lett. **10**, 565 (1985).

[29] P. B. Corkum, C. Rolland, and T. Srinivasan-Rao, Phys. Rev. Lett. **57**, 2268 (1986); P. B. Corkum and C. Rolland, IEEE J. Quantum Electron. **25**, 2634 (1989).

[30] G. S. McDonald, G. H. C. New, L. L. Losev, and A. P. Lutsenko, J. Phys. B **30**, L719 (1997).

[31] A. Brodeur and S. L. Chin, J. Opt. Soc. Am. B **16**, 637 (1999).

[32] C. A. Kapetanakos, B. Hafizi, H. M. Milchberg, P. Sprangle, R. F. Hubbard, and A. Ting, IEEE J. Quantum Electron. **35**, 565 (1999); C. A. Kapetanakos, B. Hafizi, P. Sprangle, R. F. Hubbard, and A. Ting, *ibid.* **37**, 641 (2001).

[33] G. R. Neil, C. L. Bohn, S. V. Benson, G. Biallas, D. Douglas, H. F. Dylla, R. Evans, J. Fugitt, A. Grippo, J. Gubeli, R. Hill, K. Jordan, G. A. Krafft, R. Li, L. Merminga, P. Piot, J. Preble, M. Shinn, T. Siggins, R. Walker, and B. Yunn, Phys. Rev. Lett. **84**, 662 (2000).

[34] G. P. Agrawal, *Nonlinear Fiber Optics*, 2nd ed. (Academic, San Diego, 1995).

[35] Y. R. Shen, *The Principles of Nonlinear Optics* (Wiley, New York, 1984).

[36] R. W. Boyd, *Nonlinear Optics* (Academic, San Diego, 1992).

[37] P. Sprangle, E. Esarey, and B. Hafizi, Phys. Rev. Lett. **79**, 1046 (1997); Phys. Rev. E **56**, 5894 (1997).

[38] P. Sprangle, E. Esarey, and A. Ting, Phys. Rev. A **41**, 4463 (1990).

[39] R. F. Fernsler and H. L. Rowland, J. Geophys. Res., [Atmos.] **101**, 29653 (1996); S. P. Slinker, A. W. Ali, and R. D. Taylor, J. Appl. Phys. **67**, 679 (1990).

[40] L. V. Keldysh, Zh. Eksp. Teor. Fiz. **47**, 1945 (1964) [Sov. Phys. JETP **20**, 1307 (1965)].

[41] C. Grey-Morgan, Rep. Prog. Phys. **38**, 621 (1975); G. M. Weyl, in *Laser-Induced Plasmas and Applications*, edited by L. J. Radziemski and D. A. Cremers (Dekker, Inc., New York, 1989).

[42] A. Talebpour, J. Yang, and S. L. Chin, Opt. Commun. **163**, 29 (1999).

[43] H. G. Muller, P. Agostini, and G. Petite, in *Atoms in Intense Laser Fields*, edited by M. Gavrilla (Academic, San Diego, 1992).

[44] P. Agostini, F. Fabre, G. Mainfray, G. Petite, and N. K. Rahman, Phys. Rev. Lett. **42**, 1127 (1979).

[45] L. V. Keldysh, Sov. Phys. JETP **20**, 1307 (1964); F. H. M. Faisal, J. Phys. B **6**, L89 (1973); H. R. Reiss, Phys. Rev. A **22**, 1786 (1980); J. Kupersztych, Europhys. Lett. **4**, 23 (1987).

[46] D. M. Volkov, Z. Phys. **94**, 250 (1935).

[47] P. B. Corkum, N. H. Burnete, and F. Brunel, Phys. Rev. Lett. **62**, 1259 (1989).

[48] C. J. McKinstrie and R. Bingham, Phys. Fluids B **4**, 2626 (1992).

[49] D. M. Pennington, M. A. Henesian, and R. W. Hellwarth, Phys. Rev. A **39**, 3003 (1989).

[50] E. Nibbering, G. Grillon, M. Franco, B. Prade, and A. Mysyrowicz, J. Opt. Soc. Am. B **14**, 650 (1997); J.-F. Ripoche, G. Grillon, B. Prade, M. Franco, E. Nibbering, R. Lange, and A. Mysyrowicz, Opt. Commun. **135**, 310 (1997).

[51] A. Brodeur, C. Y. Chien, F. A. Ilkov, S. L. Chin, O. G. Kosareva, and V. P. Kandidov, Opt. Lett. **22**, 304 (1997).

[52] P. Sprangle and B. Hafizi, Phys. Plasmas **6**, 1683 (1999).

[53] P. Sprangle, A. Ting, and C. M. Tang, Phys. Rev. A **36**, 2773 (1987).

[54] P. Sprangle, B. Hafizi, and J. R. Peñano, Phys. Rev. E **61**, 4381 (2000).

[55] P. Sprangle, A. Zigler, and E. Esarey, Appl. Phys. Lett. **58**, 346 (1991).

[56] R. F. Hubbard, P. Sprangle, T. G. Jones, C. I. Moore, A. Ting, B. Hafizi, D. Kaganovich, J. R. Peñano, D. Gordon, T. M. Antonsen, A. Zigler, and P. Mora, in *Proceedings of the 2001 Particle Accelerator Conference*, edited by P. Lucas and S. Webber (IEEE, Piscataway, NJ, 2001), p. 3990.

[57] F. Shimizu, Phys. Rev. Lett. **19**, 1097 (1967).

[58] In *Laser Remote Chemical Analysis*, edited by R. M. Measures, Chemical Analysis Vol. 94 (Wiley, New York, 1988); D. K. Killinger and N. Menyuk, Science **235**, 37 (1987).

[59] V. S. Averbakh, A. I. Makarov, and V. I. Talanov, Sov. J. Quantum Electron. **8**, 472 (1978).

[60] M. Rokni and A. Flusberg, IEEE J. Quantum Electron. **22**, 1102 (1986).

[61] N. Bloembergen *et al.*, Rev. Mod. Phys. **59**, S1 (1987).

[62] N. A. Kurnit and D. E. Watkins, Los Alamos National Laboratory Report No. LAUR 87-0097, 1987 (unpublished).

[63] A. P. Hickman, J. A. Paisner, and W. K. Bischel, Phys. Rev. A **33**, 1788 (1986).

[64] J. R. Ackerhalt and P. Milonni, Phys. Rev. A **33**, 3185 (1986).

[65] G. S. McDonald, G. H. C. New, L. L. Losev, A. P. Lutsenko, and M. Shaw, Opt. Lett. **19**, 1400 (1994).

[66] K. S. Syed, G. S. McDonald, and G. H. C. New, J. Opt. Soc. Am. B **17**, 1366 (2000).

[67] M. G. Raymer, J. Mostowski, and J. L. Carlsten, Phys. Rev. A **19**, 2304 (1979).

[68] K. J. Blow and D. Wood, IEEE J. Quantum Electron. **25**, 2665 (1989); R. H. Stolen, J. P. Gordon, W. J. Tomlinson, and H. A. Haus, J. Opt. Soc. Am. B **6**, 1159 (1989).
[69] A. P. Hickman and W. K. Bischel, Phys. Rev. A **37**, 2516 (1988).
[70] P. Milonni and J. H. Eberly, *Lasers* (Wiley, New York, 1988).
[71] N. E. Andreev, L. M. Gorbunov, V. I. Kirsanov, K. Nakajima, and A. Ogata, Phys. Plasmas **4**, 1145 (1997); P. Sprangle, B. Hafizi, J. R. Penano, R. F. Hubbard, A. Ting, A. Zigler, and T. M. Antonsen, Jr., Phys. Rev. Lett. **85**, 5110 (2000).